7 Orbital Ordering

Eva Pavarini
Institute for Advanced Simulation
Forschungszentrum Jülich GmbH

Contents

1   Introduction

The term *orbital ordering* (OO) indicates the emergence of a broken symmetry state in which localized occupied orbitals form a regular pattern, in a similar way as spins do in magnetically ordered structures. Orbital ordering phenomena typically occur in Mott insulators with *orbital degrees of freedom*; for transition-metal compounds, the main focus of this lecture, the latter stem from the partially filled d shells of the transition metal. The perhaps most representative case is the perovskites $KCuF_3$, shown in Fig. 1. In first approximation $KCuF_3$ is cubic (O_h point group) with Cu^{2+} at the center of a regular octahedron of F^- ions (anions), enclosed in a cage of K^+ (cations). Due to O_h symmetry at the Cu site, the d manifold, 5-fold degenerate for free Cu^{2+}, splits into a t_{2g} triplet (xz, yz, xy), lower in energy, and a e_g doublet ($x^2 - y^2$ and $3z^2 - r^2$); the electronic configuration of the Cu^{2+} ion is thus $t_{2g}^6 e_g^3$ (one hole). The t_{2g} states are completely filled and do not play any active role in OO; instead, electrons in the e_g^3 configuration have orbital degeneracy $d = 2$. Making an analogy with spin degrees of freedom, they behave as an effective $\tau = 1/2$ *pseudospin*; in this view, one of the two e_g states, say $|x^2 - y^2\rangle$, plays the role of the pseudospin up, $|\nearrow\rangle$, and the other one, $|3z^2 - r^2\rangle$, of the pseudospin down, $|\searrow\rangle$. The two pseudospin states are degenerate and, by symmetry, one could expect them to be equally occupied. In reality the symmetry is broken and $KCuF_3$ is orbitally ordered with the orbital structure shown in Fig. 1; depicted are the empty (hole) e_g states at each Cu site. Furthermore, the system exhibits a *co-operative Jahn-Teller distortion*, also shown in Fig. 1, with long and short Cu-F bonds alternating in the **ab** plane. Indeed, the two phenomena – electronic orbital ordering and structural Jahn-Teller distortion – are concurrent; it is therefore difficult to say which one is the cause and which one is, instead, the effect. The second paradigmatic system showing OO is $LaMnO_3$ (ion Mn^{3+}, configuration $3d^4$), the mother compound of colossal magnetoresistance manganites, also a perovskite. Due to the Hund's rule coupling J, the actual electronic configuration of Mn^{3+} is $t_{2g}^3 e_g^1$. The half-filled t_{2g}^3 state has no orbital degeneracy; the only orbital degrees of freedom are, as for $KCuF_3$, those associated with e_g electrons. Again, the system is orbitally ordered and orbital ordering goes hand in hand with the co-operative Jahn-Teller distortion. Among t_{2g} systems, i.e., materials with partially filled t_{2g} shells, classical examples of orbitally-ordered crystals are the perovskites $LaTiO_3$ and $YTiO_3$ (configuration t_{2g}^1), $LaVO_3$ and YVO_3 (t_{2g}^2), and Ca_2RuO_4 (t_{2g}^4); in these cases the t_{2g} electrons behave as a orbital pseudospin $\tau = 1$. Although this is not a prerequisite for orbital ordering, as we have seen, many orbitally-ordered materials are perovskites; for this reason in the present lecture we will use the perovskite structure as representative.

The origin of orbital ordering has been investigated for decades. One of the problems in clarifying its nature is that, while magnetic order can be directly probed, e.g., via neutron scattering experiments, orbital ordering is typically only indirectly observed. Indeed, its principal hallmark is the presence of the co-operative Jahn-Teller distortion itself. Identifying the origin of orbital ordering is thus intimately related to finding the cause of the co-operative Jahn-Teller distortion. In this lecture I will illustrate the two main mechanisms [1, 2] which have been proposed as possible explanation for OO phenomena, the classical Jahn-Teller effect [1], perhaps
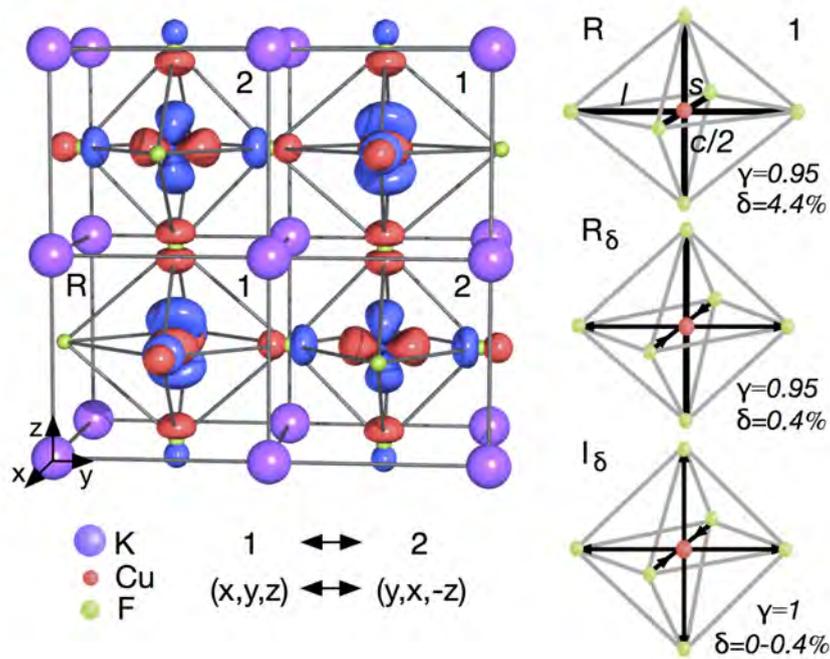
Fig. 1: *Crystal structure, distortions, and orbital order in KCuF$_3$. Cu is at the center of F octahedra enclosed in a K cage. The conventional cell is tetragonal with axes $\mathbf{a}$, $\mathbf{b}$, $\mathbf{c}$. The pseudocubic axes $\mathbf{x}$, $\mathbf{y}$, $\mathbf{z}$ pointing towards neighboring Cu are shown in the corner. Short (s) and long (l) CuF bonds alternate between $\mathbf{x}$ and $\mathbf{y}$ along all pseudocubic axes (co-operative Jahn-Teller distortion). The distortions are measured by $\delta = (l - s)/(l + s)/2$ and $\gamma = c/a\sqrt{2}$. R is the experimental structure ($\gamma = 0.95$, $\delta = 4.4\%$), R_δ ($\gamma = 0.95$) and I_δ ($\gamma = 1$) two ideal structures with reduced distortions. In the I_0 structure the cubic crystal-field at the Cu site splits the $3d$ manifold into a t_{2g} triplet and a e_g doublet. In the R structure, site symmetry is lowered further by the tetragonal compression ($\gamma < 1$) and the Jahn-Teller distortion ($\delta \neq 0$). The figure shows the highest-energy d orbital. From Ref. [3].*

enhanced by Coulomb repulsion [4], and Kugel-Khomskii superexchange [2]. Kanamori well illustrated the first mechanism in an influential work [1] in 1960; the main idea is that electron-phonon coupling yields a static Jahn-Teller distortion, which lowers the symmetry of the system and produces a crystal-field splitting. As a consequence, electrons preferably occupy the lower energy states, giving rise to a periodic pattern of occupied orbitals. This is self-evident in the limit in which the crystal-field splitting is very large, let us say, larger than the bandwidth; the lower-energy states at each site will be clearly the first ones to be occupied. If, however, the bandwidth is large in comparison with the crystal-field splitting, the hopping integrals can strongly reduce such a tendency to orbital ordering. A natural question thus arises at this point. How large should the crystal-field splitting be to give rise to a orbitally-ordered state? To answer this question we have to remind ourselves that transition-metal systems with partially filled d shells are also typical examples of strongly-correlated materials. Their low-energy properties are believed to be well described by a generalized multi-band *Hubbard model*

$$\hat{H} = \hat{H}_0 + \hat{H}_U,$$

the sum over a one-electron term $\hat{H}_0$ describing the transition-metal d bands and a Coulomb electron-electron repulsion term $\hat{H}_U$. The one-electron term is

$$\hat{H}_0 = -\sum_{ii'}\sum_{\sigma}\sum_{mm'} t^{i,i'}_{mm'}\, c^{\dagger}_{im\sigma}c_{im'\sigma}\,,$$

where $c^{\dagger}_{im\sigma}$ creates an electron at site i with spin σ and orbital quantum number m, and the parameter $t^{i,i'}_{mm'}$ are the hopping integrals ($i \neq i'$) or the crystal-field splittings ($i = i'$). The Coulomb repulsion can be written as

$$\hat{H}_U = \frac{1}{2}\sum_{i}\sum_{\sigma\sigma'}\sum_{m_\alpha m'_\alpha}\sum_{m_\beta m'_\beta} U_{m_\alpha m_\beta m'_\alpha m'_\beta}\, c^{\dagger}_{im_\alpha\sigma}c^{\dagger}_{im_\beta\sigma'}c_{im'_\beta\sigma'}c_{im'_\alpha\sigma}\,.$$

The elements the Coulomb interaction tensor, $U_{m_\alpha m_\beta m'_\alpha m'_\beta}$, can be expressed in terms of the Slater integrals[1] labeled as F_0, F_2 and F_4. Here we will restrict the discussion to the e_g or t_{2g} manifolds only. In this case, in the basis of real harmonics, the Hubbard model takes the form

$$\begin{aligned}
\hat{H} =& -\sum_{ii'}\sum_{\sigma}\sum_{mm'} t^{i,i'}_{mm'}\, c^{\dagger}_{im\sigma}c_{im'\sigma} + U\sum_{i}\sum_{m}\hat{n}_{im\uparrow}\hat{n}_{im\downarrow} \\
&+ \frac{1}{2}\sum_{i}\sum_{\sigma\sigma'}\sum_{m\neq m'}(U - 2J - J\delta_{\sigma,\sigma'})\,\hat{n}_{im\sigma}\hat{n}_{im'\sigma'} \\
&- J\sum_{i}\sum_{m\neq m'}\left[c^{\dagger}_{im\uparrow}c^{\dagger}_{im\downarrow}c_{im'\uparrow}c_{im'\downarrow} + c^{\dagger}_{im\uparrow}c_{im\downarrow}c^{\dagger}_{im'\downarrow}c_{im'\uparrow}\right],
\end{aligned} \tag{1}$$

where m, m' are here either t_{2g} or e_g states, $U_{mm'mm'} = U_{m,m'} = U - 2J(1 - \delta_{m,m'})$ and, for $m \neq m'$, $U_{mm'm'm} = J_{m,m'} = J$. The last two terms describe the pair-hopping and spin-flip processes ($U_{mmm'm'} = J_{m,m'}$ if we use a basis of real harmonics, while for spherical harmonics $U_{mmm'm'} = 0$). Finally, $U = U_0$ and $J = J_1$ (t_{2g} electrons) or $J = J_2$ (e_g electrons), with

$$U_0 = F_0 + \frac{8}{5}\mathcal{J}_{\text{avg}}$$

$$\mathcal{J}_{\text{avg}} = \frac{5}{7}\frac{1}{14}(F_2 + F_4)$$

$$J_1 = \frac{3}{49}F_2 + \frac{20}{9}\frac{1}{49}F_4$$

$$J_2 = -2\mathcal{J}_{\text{avg}} + 3J_1\,.$$

In strongly correlated systems described by a Hamiltonian of type (1) it turns out that a small crystal-field splitting, a fraction of the bandwidth, is sufficient to produce orbital order even at high temperature. This happens because the Coulomb repulsion effectively enhances it, while suppressing orbital fluctuations [4]. Hence, the mechanism illustrated by Kanamori becomes very efficient in the presence of strong correlations (small t/U limit, the typical limit for Mott insulators; here t is an average hopping integral). This is, however, not the end of the story:

---

[1]For a pedagogical introduction see, e.g, Ref. [5], or the lecture of Robert Eder in the present book.
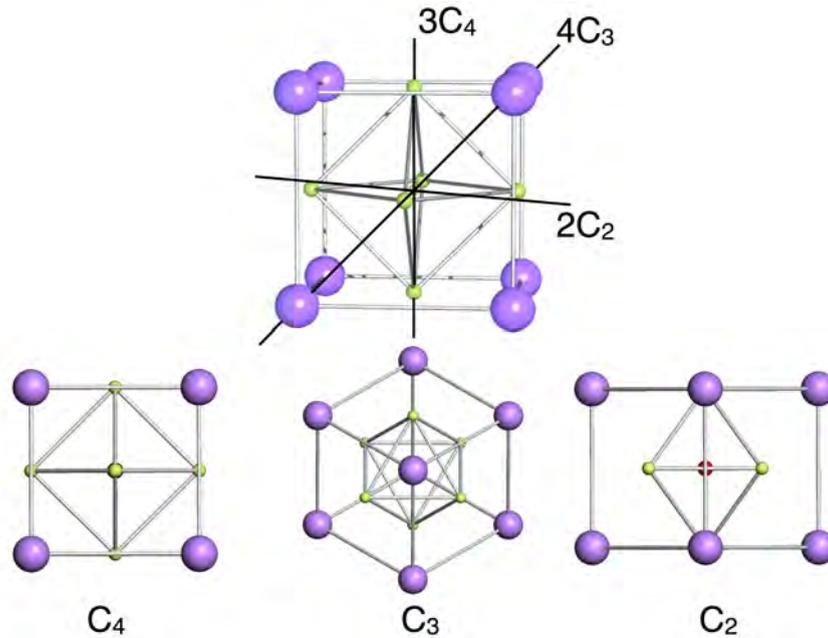
Fig. 2: *The unit cell of a cubic perovskite ABC_3 and its symmetry axes; the lattice constant is a. The transition metal B (red) is at $(0,0,0)$; the ligands C (green) are located at $(\pm a/2, 0, 0)$, $(0, \pm a/2, 0)$, $(0, 0, \pm a/2)$ and form an octahedron; the cations A are located at $(\pm a/2, \pm a/2, \pm a/2)$, $(\pm a/2, \mp a/2, \pm a/2)$, $(\mp a/2, \pm a/2, \pm a/2)$, $(\pm a/2, \pm a/2, \mp a/2)$ and form a cube. The bottom figures illustrate the rotational symmetries of the cell.*

Coulomb electron-electron interaction provides, in addition, an alternative explanation of the origin of orbital ordering. In a seminal work, Kugel and Khomskii [2] have shown in 1973 that, in the presence of orbital degeneracy, many-body effects can produce orbital ordering even in the absence of a static distortion, i.e., of a crystal-field splitting. This happens via electronic spin-orbital superexchange, the effective low-energy interaction which emerges, in the small t/U limit, from the orbitally-degenerate Hubbard model. In this picture, the co-operative Jahn-Teller distortion is rather the consequence than the cause of orbital order. The predictions of the two theories for what concerns, e.g., the final broken-symmetry structure, are basically identical; thus it is very hard to determine which of the two mechanisms, Jahn-Teller effect or Kugel-Khomskii superexchange, dominates in real systems. In the last part of the lecture we will see how the problem was recently solved [3, 6] by using a new theoretical approach based on the local-density-approximation + dynamical mean-field theory (LDA+DMFT) [7, 8] method. For the representative materials $KCuF_3$ and $LaMnO_3$, it was shown that Kugel-Khomskii superexchange alone, although strong, cannot explain the presence of the Jahn-Teller distortion above 350 K ($KCuF_3$) [3] and 650 K ($LaMnO_3$) [6]; experimentally, however, the distortion persists in both systems basically up to the melting temperature. This leads to the conclusion that a mechanism directly generating a static crystal-field splitting, such as the standard Jahn-Teller effect, is necessary to explain the experimental findings.

2   Cubic crystal-field splitting

Let us consider a system with the ideal cubic perovskite structure ABC_3, shown in Fig. 2, where B is the transition metal with partially filled d shell. The site symmetry at a B site is cubic; as we mentioned before, d states split into e_g and t_{2g} at a site with cubic symmetry. Let us understand how exactly this happens. For a free ion, the potential $v_R(\boldsymbol{r})$ which determines the one-electron energies is rotationally invariant, i.e., it has symmetry $O(3)$. This means that all one-electron states within a given l shell are degenerate, as it happens in the case of hydrogen-like atoms. When the same ion is inside a molecule or a solid, $v_R(\boldsymbol{r})$ has in general lower symmetry, the symmetry corresponding to a finite point group.[2] Thus one-electron states within a given shell l, degenerate for the free atom, can split. The symmetry reduction arises from the *crystal field*; the latter has two components, the Coulomb potential generated by the surrounding charged ions, dominant in ionic crystals, and the *ligand field* due to the bonding neighbors. In this section we will analyze the first contribution; the covalent contribution to the crystal-field splitting is discussed in the next section. Both effects give rise to a similar splitting of levels, and which contribution dominates depends on the system.

Let us thus assume that the crystal is perfectly ionic and that the ions can be treated as point charges q_α (point-charge model). Then, the one-electron potential can be written as

$$v_R(\boldsymbol{r}) = \sum_\alpha \frac{q_\alpha}{|\boldsymbol{R}_\alpha - \boldsymbol{r}|} = v_0(r) + \sum_{\alpha \neq 0} \frac{q_\alpha}{|\boldsymbol{R}_\alpha - \boldsymbol{r}|} = v_0(r) + v_c(\boldsymbol{r}), \tag{2}$$

where $\boldsymbol{R}_\alpha$ are the positions of the ions and q_α their charges. The term $v_0(r)$ is the ionic central potential at site $\boldsymbol{R}_0$, and has spherical symmetry. The term $v_c(\boldsymbol{r})$ is the electric field generated at a given site $\boldsymbol{R}_0$ by all the surrounding ions in the crystal and it is called *crystal-field potential*. For the perovskite structure ABC_3 we are interested in the crystal-field potential at the site of the transition metal, B. Let us first assume that only the contribution of nearest neighbors (the negative C ions, typically oxygens or fluorines) is relevant. The six C ions are located at positions $(\pm d_C, 0, 0), (0, \pm d_C, 0), (0, 0, \pm d_C)$ and have all the same charge q_C, while the B ion is at $(0, 0, 0)$; in terms of a, the cubic lattice constant, $d_C = a/2$. Then we can write the potential around ion B as

$$v_R(\boldsymbol{r}) = \frac{q_B}{r} + \frac{q_C}{d_C} \left[\Delta v\left(\frac{x}{d_C}; \frac{r}{d_C}\right) + \Delta v\left(\frac{y}{d_C}; \frac{r}{d_C}\right) + \Delta v\left(\frac{z}{d_C}; \frac{r}{d_C}\right) \right]$$

where

$$\Delta v(\xi; \rho) = \frac{1}{\sqrt{1+\rho^2}} \left[\frac{1}{\sqrt{1 + \frac{2\xi}{1+\rho^2}}} + \frac{1}{\sqrt{1 - \frac{2\xi}{1+\rho^2}}} \right].$$

Via the Taylor expansion

$$\frac{1}{\sqrt{1+\eta}} \sim 1 - \frac{1}{2}\eta + \frac{3}{8}\eta^2 - \frac{5}{16}\eta^3 + \frac{35}{128}\eta^4 + \dots$$

---

[2]For a concise introduction to group theory see, e.g., Ref. [9], chapter 6.

we can find the approximate expression of $\Delta v(\xi; \rho)$ for small ξ, i.e., close to ion B; the first contribution with less than spherical symmetry is

$$v_{\text{oct}}(\boldsymbol{r}) = \frac{35}{4}\frac{q_C}{d^5}\left(x^4 + y^4 + z^4 - \frac{3}{5}r^4\right) = D\left(x^4 + y^4 + z^4 - \frac{3}{5}r^4\right).$$

We can rewrite this potential as

$$v_{\text{oct}}(\boldsymbol{r}) = \frac{7\sqrt{\pi}}{3}\frac{q_C}{d^5}r^4\left[Y_0^4(\theta,\phi) + \sqrt{\frac{5}{14}}\left(Y_4^4(\theta,\phi) + Y_{-4}^4(\theta,\phi)\right)\right], \tag{3}$$

where

$$Y_0^4(\theta,\phi) = \frac{3}{16}\frac{1}{\sqrt{\pi}}\left(35\cos^4\theta - 30\cos^2\theta + 3\right) = \frac{3}{16}\frac{1}{\sqrt{\pi}}\frac{35z^4 - 30z^2r^2 - 3r^4}{r^4},$$

$$Y_{\pm4}^4(\theta,\phi) = \frac{3}{16}\sqrt{\frac{35}{2\pi}}\sin^4\theta e^{\pm4i\phi} = \frac{3}{16}\sqrt{\frac{35}{2\pi}}\frac{(x\pm iy)^4}{r^4}.$$

To obtain the crystal field due to the cubic cage of cations A (with charge q_A), shown in Fig. 2 we repeat the same calculation; the main difference is that there are eight A ions, located at positions of type $(\pm d_A, \pm d_A, \pm d_A),(\mp d_A, \pm d_A, \pm d_A), (\pm d_A, \mp d_A, \pm d_A), (\pm d_A, \pm d_A, \mp d_A)$ with $d_A = a/2$. By following the same procedure that we used for B octahedron, one can show that

$$v_{\text{cube}}(\boldsymbol{r}) = -\frac{8}{9}\frac{q_A}{q_C}\left(\frac{d_A}{d_C}\right)^5 v_{\text{oct}}(\boldsymbol{r}),$$

i.e., $v_{\text{cube}}(\boldsymbol{r})$ has the same form as $v_{\text{oct}}(\boldsymbol{r})$; this happens because a cube and an octahedron are dual polyhedra[3] and have therefore the same symmetry properties. If $q_A/q_C > 0$, $v_{\text{cube}}(\boldsymbol{r})$ has opposite sign than $v_{\text{oct}}(\boldsymbol{r})$; in the case of a perovskite, however, A positions are occupied by cations, i.e., positive ions; thus the crystal field due to the A cage has the same sign of the crystal field generated by the B octahedron.

The crystal-field potential $v_c(\boldsymbol{r})$ lowers the site symmetry and can therefore split the $(2l+1)$-fold degeneracy of the atomic levels. To calculate how the l manifold splits, we use two approaches. The first is exact and based on group theory. We assume for simplicity that the symmetry is only O (group of the proper rotations which leave a cube invariant); using the full symmetry group of the cube, $O_h = O \otimes C_i$ (where C_i is the group made by the identity and the inversion) does not change the result, because the spherical harmonics are all either even or odd. The character table of group O is given by

partner	functions	O	E	$8C_3$	$3C_2$	$6C_2'$	$6C_4$
	$(x^2+y^2+z^2)$	A_1	1	1	1	1	1
		A_2	1	1	1	-1	-1
	$(x^2-y^2, 3z^2-r^2)$	E	2	-1	2	0	0
(R_x, R_y, R_z)	(x,y,z)	T_1	3	0	-1	-1	1
	(xy, xz, yz)	T_2	3	0	-1	1	-1

$$\tag{4}$$

---

[3]Every polyhedron has a dual which can be obtained by exchanging the location of faces and vertices.

Let us explain this table. The first line yields the group, here O, and the symmetry operations of the group, collected in classes $\mathcal{C}_k$, here $\{E\}, \{C_3\}, \{C_2\}, \{C_2'\}, \{C_4\}$. For each class only a representative element is given and the number N_k in front of this element yields the number of operations in the class; for example $8C_3$ indicates 8 symmetry operations in class $\{C_3\}$. The symmetry operation C_n is an anticlockwise rotation of an angle $\alpha = 2\pi/n$. For a finite group with h elements, the h group operations $\{O(g)\}$ can be expressed as h matrices $\{\Gamma(g)\}$ acting on an invariant linear space; the basis of this space, $\{|m\rangle\}$, can be, for example, a finite set of linearly independent functions, such as the spherical harmonics with angular quantum number l. The collection of matrices $\{\Gamma(g)\}$ is a *representation* of the group; the dimension of the invariant linear space yields also the dimension of the matrices, i.e., the *dimensionality* of the representation. Each group has infinitely many possible representations, but some sets are special and play the role of an orthonormal basis in a space of vectors; they are called *irreducible*. If G is the group of operations which leave the Hamiltonian invariant, the irreducible representations of G can be used to classify all eigenstates of the Hamiltonian; eigenstates which build a basis for different irreducible representations are mutually orthogonal and have typically (leaving the cases of accidental degeneracy and hidden symmetry aside) different energies. The irreducible representations Γ_i of group O are listed in the first column of Table 4, below the group name; they are A_1 (trivial representation, made of 1-dimensional identity matrices), A_2, also 1-dimensional, E, two-dimensional, and T_1 and T_2, both three-dimensional. The numbers appearing in Table 4 are the characters $\chi_i(g)$, defined as

$$\chi_i(g) = \mathrm{Tr}\,\Gamma_i(g) = \sum_m \langle m|\Gamma_i(g)|m\rangle = \sum_m \Gamma_i^{mm}(g)\,.$$

For a given representation (corresponding to a line of Table 4) the character for a specific element can be found below the corresponding class label (columns of Table 4); all elements in the same class have the same character. Thus the second column of the character table, showing the character of the identity, yields also the dimensionality d_i of the representation itself. Next we calculate the characters of the matrix representation Γ^l constructed using spherical harmonics with angular quantum number l as a basis. An easy way to do this is to assume that the rotation axis is also the axis of quantization, i.e., $\hat{z}$; the characters do not depend on the actual direction of the quantization axis but only on the angle α of rotation. Thus for $O(g) = C_\alpha$ we have

$$C_\alpha\,Y_m^l(\theta,\phi) = Y_m^l(\theta,\phi-\alpha) = e^{-im\alpha}\,Y_m^l(\theta,\phi)$$

$$\Gamma_{mm'}^l(C_\alpha) = \delta_{mm'}e^{-im\alpha}.$$

This yields the following expression for the character

$$\chi^l(C_\alpha) = \sum_{m=-l}^{l} e^{-im\alpha} = \frac{\sin(l+\frac{1}{2})\alpha}{\sin\frac{\alpha}{2}}\,.$$

The characters for representations Γ^l are therefore

O	E	$8C_3$	$3C_2$	$6C_2$	$6C_4$
$\Gamma^0 = \Gamma^s$	1	1	1	1	1
$\Gamma^1 = \Gamma^p$	3	0	-1	-1	1
$\Gamma^2 = \Gamma^d$	5	-1	1	1	-1
$\Gamma^3 = \Gamma^f$	7	1	-1	-1	-1

In spherical symmetry (group $O(3)$) representations Γ^l are irreducible. In cubic symmetry (group O), instead, the Γ^l can be reducible, i.e., they can be written as the tensorial sum $\oplus$ of irreducible representations of the group O. The various components can be found by using the orthogonality properties of irreducible representations, which lead to the decomposition formula

$$\Gamma^l = \bigoplus_i a_i \Gamma_i \qquad \text{with} \quad a_i = \langle \Gamma_i | \Gamma^l \rangle = \frac{1}{h} \sum_g [\chi_i(g)]^* \chi^l(g), \qquad (5)$$

where h, the number of elements in the group, is 24 for group O. Hereafter the symmetry representations of electronic states are written in lower case to distinguish them from capital letters which we will use later for labeling vibrational modes. We find

$$\begin{aligned}
\Gamma^s &= a_1 \\
\Gamma^p &= t_1 \\
\Gamma^d &= e \oplus t_2 \\
\Gamma^f &= a_2 \oplus t_1 \oplus t_2 \, .
\end{aligned}$$

Thus, in cubic symmetry, the s- and the p-functions do not split, because the a_1 irreducible representation is one-dimensional and the t_1 irreducible representation is 3-dimensional. Instead, d-functions split into a doublet and a triplet, and f-functions into a singlet and two triplets. To determine which functions $\{|m\rangle_i\}$ form a basis (a so-called set of *partner functions*) for a specific irreducible representation Γ_i we can, e.g., use the projector for that representation

$$\hat{\mathcal{P}}_i = \frac{d_i}{h} \sum_g [\chi_i(g)]^* O(g). \qquad (6)$$

In our case, we can read directly the partner functions $\{|m\rangle_i\}$ for a given irreducible representation of the group O in the first column of Table 4, on the left. In short, for representation e partner functions are $(x^2 - y^2, \, 3z^2 - r^2)$ and for representation t_2 they are $(xy, \, xz, \, yz)$. A small step is still missing: As we already mentioned, the full symmetry of the B site is O_h, and the group O_h can be obtained as direct product, $O_h = O \otimes C_i$; with respect to O, group O_h has twice the number of elements and classes, and thus twice the number of irreducible representations. The latter split into even ($a_{1g}, a_{2g}, e_g, t_{1g}, t_{2g}$) and odd ($a_{1u}, a_{2u}, e_u, t_{1u}, t_{2u}$). All d-functions are even, and therefore $x^2 - y^2$ and $3z^2 - r^2$ are partners functions for the e_g irreducible representation, while xy, xz, yz are partner functions for the t_{2g} irreducible representation. Summarizing,

t_{2g} states $(xy, xz,$ and $yz)$ and e_g states $(x^2 - y^2$ and $3z^2 - r^2)$ have in general (again excluding the cases of accidental degeneracy and hidden symmetry) different energy.

Group theory tells us *if* the degenerate $2l + 1$ levels split at a given site in a lattice, but not of *how much* they do split, and which orbitals are higher in energy. We can, however, calculate the crystal-field splitting approximately using the potential (3) as a perturbation. This is the second approach previously mentioned; differently from group theory, it is not exact, but it gives us an estimate of the size of the effect and the sign of the splitting. For d states we can calculate the elements of the octahedral potential $v_{\rm oct}(\boldsymbol{r})$ in the basis of atomic functions $\psi_{nlm}(\rho, \theta, \phi) = R_{nl}(\rho)Y_l^m(\theta, \phi)$, where $R_{nl}(\rho)$ is the radial part, $\rho = Zr$, Z is the atomic number, $Y_l^m(\theta, \phi)$ a spherical harmonic, and n the principal quantum number (Appendix B). We obtain

$$\langle \psi_{n20} \ |\hat{v}_{\rm oct}|\psi_{n20} \ \rangle = +6Dq \qquad\qquad \langle \psi_{n2\pm1}|\hat{v}_{\rm oct}|\psi_{n2\pm1}\rangle = -4Dq$$

$$\langle \psi_{n2\pm2}|\hat{v}_{\rm oct}|\psi_{n2\pm2}\rangle = + \ Dq \qquad\qquad \langle \psi_{n2\pm2}|\hat{v}_{\rm oct}|\psi_{n2\mp2}\rangle = +5Dq$$

where $Dq = q_C\langle r^4\rangle/6d_C^5$ and $\langle r^k\rangle = \int r^2 dr \ r^k \ R_{n2}^2(Zr)$. The crystal-field splitting between e_g and t_{2g}-states can be then obtained by diagonalizing the crystal-field matrix

$$H_{\rm CF} = \begin{pmatrix} Dq & 0 & 0 & 0 & 5Dq \\ 0 & -4Dq & 0 & 0 & 0 \\ 0 & 0 & 6Dq & 0 & 0 \\ 0 & 0 & 0 & -4Dq & 0 \\ 5Dq & 0 & 0 & 0 & Dq \end{pmatrix}.$$

We find two degenerate e_g eigenvectors with energy $6Dq$

$$|\psi_{n20}\rangle = |3z^2 - r^2\rangle,$$

$$\frac{1}{\sqrt{2}}\left[|\psi_{n22}\rangle + |\psi_{n2-2}\rangle\right] = |x^2 - y^2\rangle,$$

and three degenerate t_{2g} eigenvectors with energy $-4Dq$

$$\frac{i}{\sqrt{2}}\left[|\psi_{n22}\rangle - |\psi_{n2-2}\rangle\right] = |xy\rangle,$$

$$\frac{1}{\sqrt{2}}\left[|\psi_{n21}\rangle - |\psi_{n2-1}\rangle\right] = |xz\rangle,$$

$$\frac{i}{\sqrt{2}}\left[|\psi_{n21}\rangle + |\psi_{n2-1}\rangle\right] = |yz\rangle.$$

The total splitting is

$$\Delta_{\rm CF} = E_{e_g} - E_{t_{2g}} = 10Dq.$$

Thus the e_g-states are actually higher in energy than the t_{2g}-states. This happens because e_g electrons point towards the negative C ions (see Fig. 3), and will therefore feel a larger Coulomb repulsion than t_{2g} electrons, which have the lobes directed between the negative C ions.
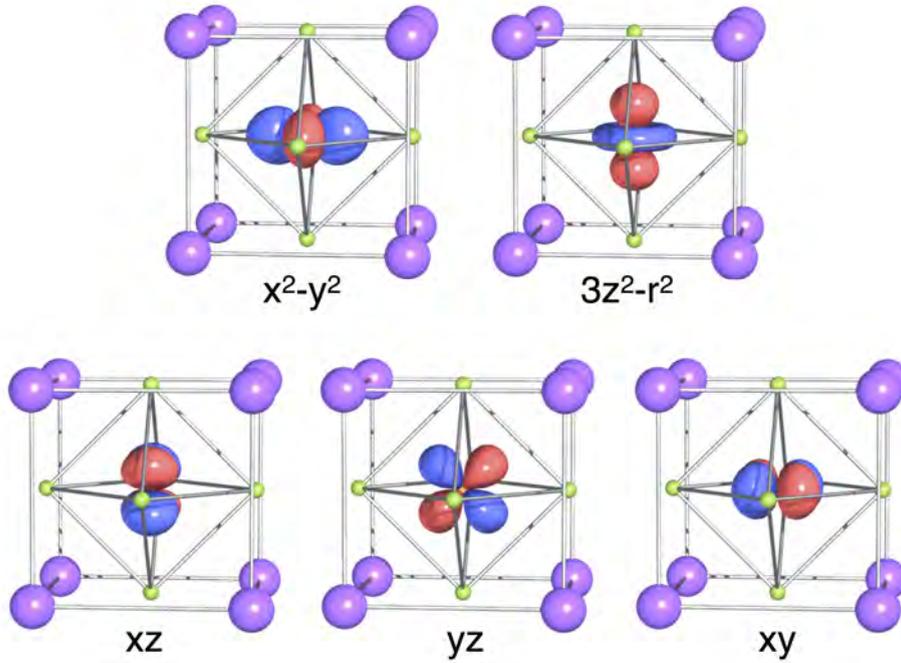
Fig. 3: *The Cu e_g and t_{2g} Wannier orbitals for the cubic perovskite $KCuF_3$, obtained from first principles calculations, using a Wannier basis that spans all bands.*

How general is, however, this result? We obtained it via a truncated Taylor expansion of the potential close to the nucleus. Does this mean that we have perhaps neglected important higher-order terms? For a generic lattice, we can expand the crystal-field potential (2) in spherical harmonics using the exact formula

$$\frac{1}{|\boldsymbol{r}_1 - \boldsymbol{r}_2|} = \sum_{k=0}^{\infty} \frac{r_<^k}{r_>^{k+1}} \frac{4\pi}{2k+1} \sum_{q=-k}^{k} Y_q^k(\theta_2, \phi_2) \overline{Y}_q^k(\theta_1, \phi_1),$$

where $r_<$ ($r_>$) is the smaller (larger) of r_1 and r_2. The crystal-field potential takes the form

$$v_c(\boldsymbol{r}) = \sum_{k=0}^{\infty} \sum_{q=-k}^{k} B_q^k Y_q^k, \tag{7}$$

where $B_q^k = (-1)^q \bar{B}_{-q}^k$. Although the series in (7) is in principle infinite, one can terminate it by specifying the wavefunctions, since

$$\langle Y_m^l | Y_q^k | Y_{m'}^l \rangle = 0 \quad \text{if} \quad k > 2l.$$

For example, for p electrons $k \leq 2$, for d-electrons, $k \leq 4$, and f electrons $k \leq 6$. Thus, for d-electrons and O_h symmetry, the terms that appear in the potential (3) are actually also the only ones to be taken into account, because all other terms yield an expectation value equal to zero. Finally, the derivation of both equations (3) and (7) presented here might let us think that the first-nearest neighbors are those that determine the crystal field. This is, however, not always the case, because Coulomb repulsion is a long-range interaction; for example, in some systems
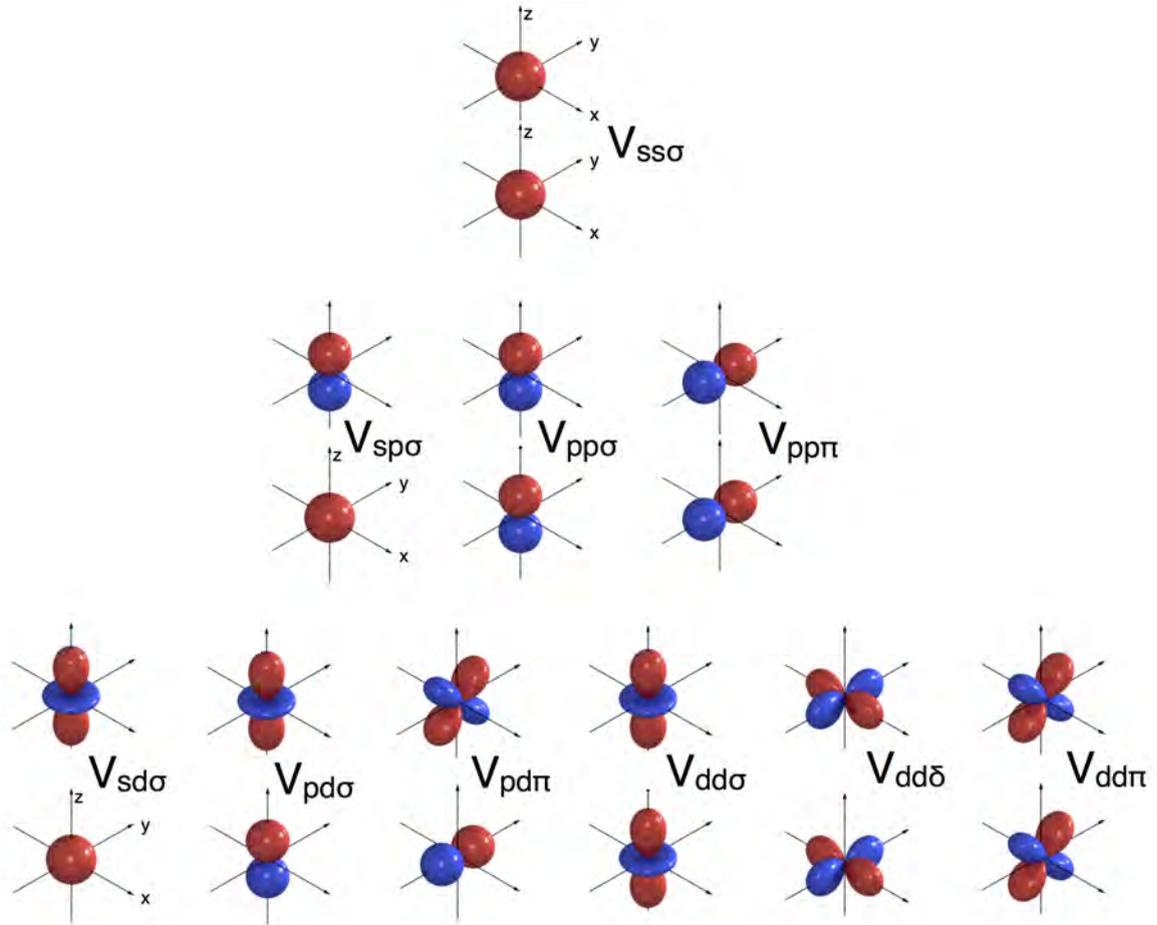
Fig. 4: *Independent Slater-Koster two-center integrals for s, p, and d atomic orbitals (Appendix B). The label σ indicates that the bonding state is symmetrical with respect to rotations about the bond axis; the label π that the bond axis lies in a nodal plane; the label δ that the bond axis lies in two nodal planes.*

the first-nearest neighbors yield cubic symmetry at a given site but further neighbors lower the symmetry.[4] Furthermore, the point-charge model discussed in this section is useful to explain the relation between crystal field and site symmetry, however yields unsatisfactory results for the crystal-field splitting in real materials. Corrections beyond the point-charge approximation turn out to be important. In addition, as we will see in the next section, in many systems the crystal field has a large, sometimes dominant, covalent contribution, the ligand field. The modern approach to calculate crystal-field splittings including the ligand-field contribution is based on material-specific potentials obtained *ab-initio* via density-functional-theory (DFT) and the associated DFT localized Wannier functions. Nevertheless, it is worth to point out the remarkable success of the point-charge model in giving qualitatively correct d crystal-field states in cubic perovskites; such a success relies on the fact that this approach, even if approximate, yields the exact symmetry of final states, i.e., the same obtained via group theory, and does not neglect any relevant (e.g., high-order) term.

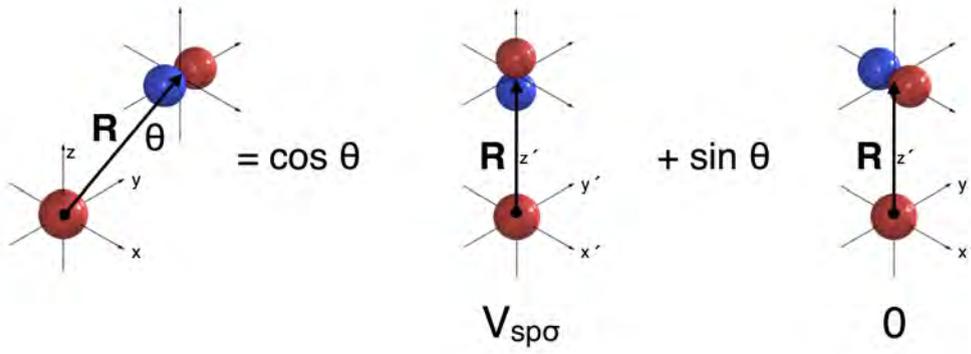[4]This means that, of course, O_h is not the actual symmetry of the site.

Fig. 5: *Illustration of the decomposition of a general s-p two-center integral in terms of $V_{sp\sigma}$.*

3   Tight-binding e_g and t_{2g} bands of cubic perovskites

In this section we will construct the bands of $KCuF_3$ in the cubic limit using tight-binding theory. Let us first remind ourselves of the crucial steps of this approach. The one-electron Hamiltonian can be written as

$$\hat{h}_e(\boldsymbol{r}) = -\frac{1}{2}\nabla^2 + \sum_{i\alpha} v(\boldsymbol{r} - \boldsymbol{T}_i - \boldsymbol{R}_\alpha) = -\frac{1}{2}\nabla^2 + v_R(\boldsymbol{r}),$$

where $\boldsymbol{R}_\alpha$ are the positions of the basis $\{\alpha\}$ atoms in the unit cell and $\boldsymbol{T}_i$ the lattice vectors. We take as a basis atomic orbitals with quantum numbers lm (we drop here the principal quantum number for convenience). For each atomic orbital we construct a Bloch state

$$\psi_{lm}^\alpha(\boldsymbol{k}, \boldsymbol{r}) = \frac{1}{\sqrt{N}} \sum_i e^{i\boldsymbol{T}_i \cdot \boldsymbol{k}} \, \psi_{lm}(\boldsymbol{r} - \boldsymbol{T}_i - \boldsymbol{R}_\alpha), \tag{8}$$

where N is the number of lattice sites. In the Bloch basis (8), the Hamiltonian and the overlap matrix are given by

$$H_{lm,l'm'}^{\alpha,\alpha'}(\boldsymbol{k}) = \langle \psi_{lm}^\alpha(\boldsymbol{k})|\hat{h}_e|\psi_{l'm'}^{\alpha'}(\boldsymbol{k})\rangle,$$

$$O_{lm,l'm'}^{\alpha,\alpha'}(\boldsymbol{k}) = \langle \psi_{lm}^\alpha(\boldsymbol{k})|\psi_{l'm'}^{\alpha'}(\boldsymbol{k})\rangle.$$

These matrices define a generalized eigenvalue problem, the solution of which yields the band structure. The Hamiltonian matrix is given by

$$H_{lm,l'm'}^{\alpha,\alpha'}(\boldsymbol{k}) = \varepsilon_{l'\alpha'}^0 \, O_{lm,l'm'}^{\alpha,\alpha'}(\boldsymbol{k}) + \Delta\varepsilon_{lm,l'm'}^\alpha \, \delta_{\alpha,\alpha'} - \frac{1}{N} \sum_{i\alpha \neq i'\alpha'} e^{i(\boldsymbol{T}_{i'} - \boldsymbol{T}_i)\cdot \boldsymbol{k}} \, t_{lm,l'm'}^{i\alpha,i'\alpha'}.$$

Here $\varepsilon_{l\alpha}^0$ are the atomic levels, and $\Delta\varepsilon_{lm,l'm'}^\alpha$ the crystal-field matrix elements

$$\Delta\varepsilon_{lm,l'm'}^\alpha = \int d\boldsymbol{r} \, \overline{\psi_{lm}}(\boldsymbol{r} - \boldsymbol{R}_\alpha)\left[v_R(\boldsymbol{r}) - v(\boldsymbol{r} - \boldsymbol{R}_\alpha)\right]\psi_{l'm'}(\boldsymbol{r} - \boldsymbol{R}_\alpha), \tag{9}$$
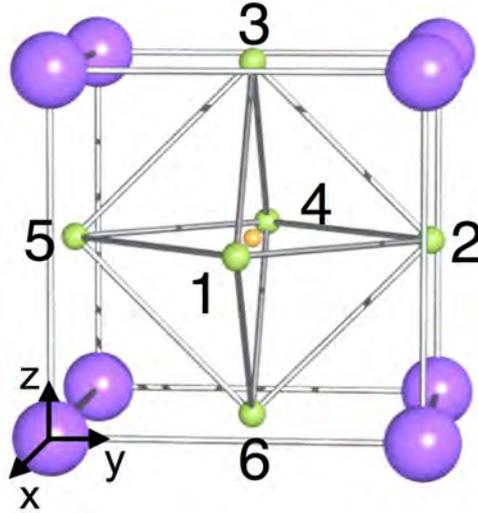
Fig. 6: *Unit cell of idealized cubic KCuF₃ with cubic axes in the left corner.*

which are two-center integrals. Finally,

$$t_{lm,l'm'}^{i\alpha,i'\alpha'} = -\int d\boldsymbol{r}\,\overline{\psi_{lm}}(\boldsymbol{r} - \boldsymbol{R}_\alpha - \boldsymbol{T}_i)\left[v_R(\boldsymbol{r}) - v(\boldsymbol{r} - \boldsymbol{R}_{\alpha'} - \boldsymbol{T}_{i'})\right]\psi_{l'm'}(\boldsymbol{r} - \boldsymbol{R}_{\alpha'} - \boldsymbol{T}_{i'}). \quad (10)$$

The hopping integrals (10) contain two- and three-center terms; if the basis is sufficiently local-
ized we can, however, neglect the three-center contributions and assume $t_{lm,l'm'}^{i\alpha,i'\alpha'} \sim -V_{lm,l'm'}^{i\alpha,i'\alpha'}$,
where

$$V_{lm,l'm'}^{i\alpha,i'\alpha'} = \int d\boldsymbol{r}\,\overline{\psi_{lm}}(\boldsymbol{r} - \boldsymbol{R}_\alpha - \boldsymbol{T}_i)v(\boldsymbol{r} - \boldsymbol{R}_\alpha - \boldsymbol{T}_i)\psi_{l'm'}(\boldsymbol{r} - \boldsymbol{R}_{\alpha'} - \boldsymbol{T}_{i'})$$

is a Slater-Koster two-center integral (Appendix B). A generic Slater-Koster two-center integral
can be expressed as a function of a few independent two-center integrals, shown in Fig. 4 for
s, p, and d-functions. Apart from the σ bond, which is the strongest, other bonds are possible;
the π bonds are made of orbitals which share a nodal plane to which the bond axis belongs,
and the δ bond, for which two nodal planes intersect in the bond axis connecting the two ions.
Fig. 5 shows how to obtain a generic two-center integral involving p and s orbitals.[5]   Let us
now consider the case of the e_g and t_{2g} bands of KCuF₃; here we assume for simplicity that the
system is an ideal cubic perovskite, shown in Fig. 6. The primitive cell contains one formula
unit (a single K cube in Fig. 1). The cubic axes are $\boldsymbol{x}$, $\boldsymbol{y}$, $\boldsymbol{z}$, and the lattice constant is a. A Cu
atom at site $\boldsymbol{R}_i$ is surrounded by two apical F atoms, F₃ at $\boldsymbol{R}_i + \frac{1}{2}\boldsymbol{z}$ and F₆ at $\boldsymbol{R}_i - \frac{1}{2}\boldsymbol{z}$, and four
planar F atoms, F₁ and F₄ at $\boldsymbol{R}_i \pm \frac{1}{2}\boldsymbol{x}$ and F₂ and F₅ at $\boldsymbol{R}_i \pm \frac{1}{2}\boldsymbol{y}$. In Fig. 7 one can see the effects
of the cubic approximation on the e_g bands: the crystal-field splitting of the e_g states is zero, the
band width slightly reduced, gaps disappear, and the dispersion relations is sizably modified.
The cubic band structure in Fig. 7 was obtained with a unit cell containing two formula units, in
order to compare it with the band structure of the experimental (Jahn-Teller distorted) structure
of KCuF₃; hence we see four (instead of two) e_g bands. The band-structure of cubic KCuF₃ for

---

[5]More details on the tight-binding approach can be found either in Ref. [9] or in the lecture of Matthew Foulkes.
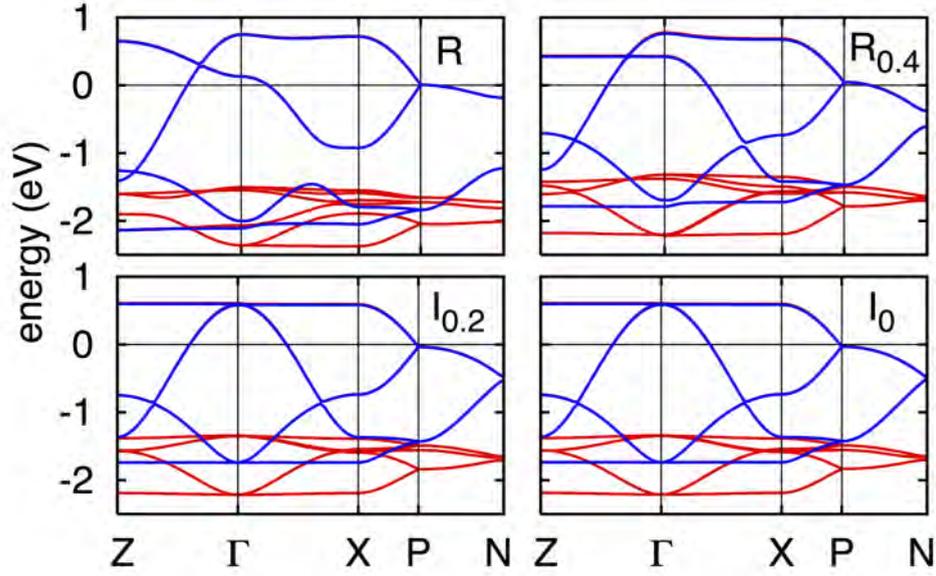
Fig. 7: *LDA e_g (blue) and t_{2g}(red) band structure of KCuF$_3$ for the experimental structure (R) and ideal structures with progressively reduced distortions (see Fig. 1). I_0: simple cubic. The unit cell used in this calculation contains two formula units. The figure is from Ref. [3].*

a cell with one formula unit is shown in Fig. 8; in the following we will refer for comparison to that figure only. Let us take as tight-binding basis the atomic $3d$ e_g orbitals for Cu and the $2p$ orbitals for F; we neglect for convenience the overlap integrals (i.e., we assume that our atomic functions are, approximately, localized *Wannier functions*). For such a tight-binding basis the only relevant Slater-Koster parameter is $V_{pd\sigma}$. The $|3z^2 - r^2\rangle_i$ and $|x^2 - y^2\rangle_i$ states of the Cu at $\boldsymbol{R}_i$ can couple via $V_{pd\sigma}$ to $|z^c\rangle_i$, the p_z orbitals of F$_3$ and F$_6$, to $|x^a\rangle_i$, the p_x orbitals of F$_1$ and F$_4$ and to $|y^b\rangle_i$, the p_y orbitals of F$_2$ and F$_5$. From the basis $|\alpha\rangle_i$ of localized atomic functions we construct the Bloch states $|\boldsymbol{k}\alpha\rangle = \frac{1}{\sqrt{N}} \sum_i e^{i\boldsymbol{k}\cdot\boldsymbol{R}_i} |\alpha\rangle_i$, and obtain the tight-binding Hamiltonian

$H^{\mathrm{TB}}_{e_g}$	$\|\boldsymbol{k}\ z^c\rangle$	$\|\boldsymbol{k}\ x^a\rangle$	$\|\boldsymbol{k}\ y^b\rangle$	$\|\boldsymbol{k}\ 3z^2 - r^2\rangle$	$\|\boldsymbol{k}\ x^2 - y^2\rangle$
$\|\boldsymbol{k}\ z^c\rangle$	ε_p	0	0	$-2V_{pd\sigma}s_z$	0
$\|\boldsymbol{k}\ x^a\rangle$	0	ε_p	0	$V_{pd\sigma}s_x$	$-\sqrt{3}V_{pd\sigma}s_x$
$\|\boldsymbol{k}\ y^b\rangle$	0	0	ε_p	$V_{pd\sigma}s_y$	$\sqrt{3}V_{pd\sigma}s_y$
$\|\boldsymbol{k}\ 3z^2 - r^2\rangle$	$-2V_{pd\sigma}\bar{s}_z$	$V_{pd\sigma}\bar{s}_x$	$V_{pd\sigma}\bar{s}_y$	ε_d	0
$\|\boldsymbol{k}\ x^2 - y^2\rangle$	0	$-\sqrt{3}V_{pd\sigma}\bar{s}_x$	$\sqrt{3}V_{pd\sigma}\bar{s}_y$	0	ε_d

$$(11)$$

where $s_\alpha = ie^{-ik_\alpha a/2} \sin k_\alpha a/2$, $\alpha = x, y, z$, $\varepsilon_p < \varepsilon_d = \varepsilon_p + \Delta_{pd}$, and $V_{pd\sigma} < 0$. If $|V_{pd\sigma}|/\Delta_{pd}$ is small, the occupied bands are F p-like, while the partially filled bands Cu e_g-like. We now calculate the bands along high-symmetry lines.[6] Along Γ-Z, the eigenvalues ε_i ($\varepsilon_i \leq \varepsilon_{i+1}$) of

---

[6]Special points: $\Gamma = (0, 0, 0)$, Z$= (0, 0, \pi/a)$, X$= (\pi/a, 0, 0)$, M$= (\pi/a, \pi/a, 0)$, R$= (\pi/a, \pi/a, \pi/a)$.
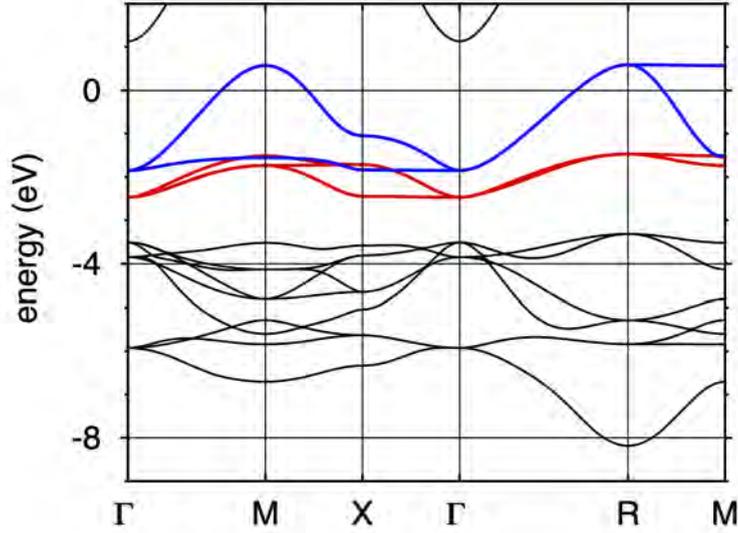
Fig. 8: *LDA band structure of cubic KCuF$_3$. The t_{2g} bands are in red and the e_g bands in blue.*

$H_{e_g}^{\mathrm{TB}}$ are

$$
\begin{aligned}
\varepsilon_2 &= \varepsilon_p \\
\varepsilon_3 &= \varepsilon_p \\
\varepsilon_4 &= \varepsilon_d \\
\varepsilon_{1,5} &= \varepsilon_p + \tfrac{1}{2}\Delta_{pd} \pm \tfrac{1}{2}\sqrt{\Delta_{pd}^2 + 16V_{pd\sigma}^2|s_z|^2}
\end{aligned}
$$

where ε_1 (sign $-$) is bonding and F z-like, while ε_5 (sign $+$) anti-bonding and Cu $3z^2 - r^2$-like. Along Γ-X, we have instead the dispersion relations

$$
\begin{aligned}
\varepsilon_2 &= \varepsilon_p \\
\varepsilon_3 &= \varepsilon_p \\
\varepsilon_4 &= \varepsilon_d \\
\varepsilon_{1,5} &= \varepsilon_p + \tfrac{1}{2}\Delta_{pd} \pm \tfrac{1}{2}\sqrt{\Delta_{pd}^2 + 16V_{pd\sigma}^2|s_x|^2}
\end{aligned}
$$

where ε_1 is bonding and F x-like, while ε_5 anti-bonding and Cu $x^2 - y^2$-like. To obtain the e_g-like bands, instead of diagonalizing $H_{e_g}^{\mathrm{TB}}$ as we have done above, we can also use the *downfolding* procedure, which, for non-interacting electrons, can be carried out exactly. This method works as follows. We divide the orbitals in passive (F p) and active (Cu d), and write the eigenvalues equation as

$$
\begin{bmatrix} H_{pp} & H_{pd} \\ H_{dp} & H_{dd} \end{bmatrix}
\begin{bmatrix} |\boldsymbol{k}\,p\rangle \\ |\boldsymbol{k}\,d\rangle \end{bmatrix}
= \varepsilon
\begin{bmatrix} I_{pp} & 0 \\ 0 & I_{dd} \end{bmatrix}
\begin{bmatrix} |\boldsymbol{k}\,p\rangle \\ |\boldsymbol{k}\,d\rangle \end{bmatrix},
$$

where H_{pp} (I_{pp}) is the Hamiltonian (identity matrix) in the p-electron space (3×3), and H_{dd} (I_{dd}) the Hamiltonian (identity matrix) in the d-electron space (2×2). By downfolding to the d sector we obtain the energy-dependent operator H_{dd}^ε, which acts in the d space only

$$
H_{dd}^\varepsilon = H_{dd} - H_{dp}(H_{pp} - \varepsilon I_{pp})^{-1}H_{pd},
$$

and a correspondingly transformed and energy-dependent basis set for the active space, $|\mathbf{k}\,d\rangle_\varepsilon$. The operator H_{dd}^ε has the same eigenvalues and eigenvectors as the original Hamiltonian. In the case of the e_g bands ($H_{dd}^\varepsilon = H_{e_g}^\varepsilon$) of KCuF$_3$

$H_{e_g}^\varepsilon$	$\|\boldsymbol{k}\,3z^2-r^2\rangle_\varepsilon$	$\|\boldsymbol{k}\,x^2-y^2\rangle_\varepsilon$
$\|\boldsymbol{k}\,3z^2-r^2\rangle_\varepsilon$	$\varepsilon_d' - 2t_\varepsilon^\sigma[\frac{1}{4}(\cos k_x a + \cos k_y a) + \cos k_z a]$	$2t_\varepsilon^\sigma[\frac{\sqrt{3}}{4}(\cos k_x a - \cos k_y a)]$
$\|\boldsymbol{k}\,x^2-y^2\rangle_\varepsilon$	$2t_\varepsilon^\sigma[\frac{\sqrt{3}}{4}(\cos k_x a - \cos k_y a)]$	$\varepsilon_d' - 2t_\varepsilon^\sigma[\frac{3}{4}(\cos k_x a + \cos k_y a)]$

$$(12)$$

where the effective parameters are

$$t_\varepsilon^\sigma = \frac{V_{pd\sigma}^2}{\varepsilon - \varepsilon_p}, \quad \varepsilon_d' = \varepsilon_d + 3t_\varepsilon^\sigma.$$

The downfolding procedure has *renormalized* the parameters ε_d of the original model (11), but also introduced a new interaction: inter-orbital coupling. Furthermore, H_{dd}^ε and the Bloch basis are now energy dependent. Along ΓZ, the eigenvalues of (12) are given implicitly by the equations $\varepsilon = \varepsilon_d + 2t_\varepsilon^\sigma - 2t_\varepsilon \cos k_z a$ (band ε_5) and $\varepsilon = \varepsilon_d$ (band ε_4); in second-order perturbation theory we find

$$t_\varepsilon^\sigma \sim t_{\varepsilon_d}^\sigma = \frac{V_{pd\sigma}^2}{\Delta_{pd}},$$

$$\varepsilon_5 \sim \varepsilon_d + 2t_{\varepsilon_d}^\sigma - 2t_{\varepsilon_d}^\sigma \cos k_z a\,.$$

From Hamiltonian (12) it is relatively easy to see that the e_g bands are 2-fold degenerate along direction Γ-R, to find the dispersion along Γ-M and R-M, and to obtain the e_g-like bands in Fig. 8. By Fourier transforming the Bloch states $|\boldsymbol{k}\,3z^2 - r^2\rangle_\varepsilon$ and $|\boldsymbol{k}\,x^2 - y^2\rangle_\varepsilon$ we can build a set of Wannier functions. They have $3z^2 - r^2$ or $x^2 - y^2$ symmetry as the atomic orbitals, and, additionally, they span, to arbitrary accuracy, the e_g bands. These Wannier functions are by construction longer range than atomic orbitals, since they have p tails on the downfolded neighboring F sites.

We can now repeat the same calculation for the t_{2g} bands. The minimal tight-binding basis is of course different with respect to the case of e_g bands. The states $|xy\rangle_i$ of the Cu ion located at $\boldsymbol{R}_i$ are coupled via $V_{pd\pi}$ to the $|y^a\rangle_i$, the p_y orbitals of F$_1$ and F$_4$ and to $|x^b\rangle_i$, the p_x orbitals of F$_2$ and F$_5$; in a similar way, $|xz\rangle_i$ is coupled via $V_{pd\pi}$ to the $|z^a\rangle_i$, the p_z orbitals of F$_1$ and F$_4$, and to the $|x^c\rangle_i$, the p_x orbitals of F$_3$ and F$_6$; finally $|yz\rangle_i$ is coupled via $V_{pd\pi}$ to the $|z^b\rangle_i$, the p_z orbitals of F$_2$ and F$_5$, and to the $|y^c\rangle_i$, the p_y orbitals of F$_3$ and F$_6$. After constructing for each $|\alpha\rangle_i$ the corresponding Bloch state, we obtain the tight-binding Hamiltonian. The latter splits into three decoupled blocks,

$H_{t_{2g}}^{\text{TB}}$	$\|\boldsymbol{k}\,y^a\rangle$	$\|\boldsymbol{k}\,x^b\rangle$	$\|\boldsymbol{k}\,xy\rangle$
$\|\boldsymbol{k}\,y^a\rangle$	ε_p	0	$2V_{pd\pi}s_x$
$\|\boldsymbol{k}\,x^b\rangle$	0	ε_p	$2V_{pd\pi}s_y$
$\|\boldsymbol{k}\,xy\rangle$	$2V_{pd\pi}\overline{s}_x$	$2V_{pd\pi}\overline{s}_y$	ε_d

and cyclic permutations of x, y, and z (and, correspondingly, of a, b, and c). In the Γ-X direction we thus find

$$\varepsilon_{2'}(\boldsymbol{k}) = \varepsilon_d$$

$$\varepsilon_5(\boldsymbol{k}) = \varepsilon_p + \frac{\Delta_{pd}}{2} + \frac{\sqrt{\Delta_{pd}^2 + 16V_{pd\pi}^2|s_x|^2}}{2}$$

$$\sim \varepsilon_d + 2t_{\varepsilon_d}^\pi - 2t_{\varepsilon_d}^\pi \cos k_x a$$

where $t_{\varepsilon_d}^\pi = V_{pd\pi}^2/\Delta_{pd}$. By downfolding the oxygen states we obtain

$H_{t_{2g}}^\varepsilon$	$\|\boldsymbol{k}\ yz\rangle_\varepsilon$	$\|\boldsymbol{k}\ xz\rangle_\varepsilon$	$\|\boldsymbol{k}\ xy\rangle_\varepsilon$
$\|\boldsymbol{k}\ yz\rangle_\varepsilon$	$\varepsilon_d'' - 2t_\varepsilon^\pi \left(\cos k_x a + \cos k_y a\right)$	0	0
$\|\boldsymbol{k}\ xz\rangle_\varepsilon$	0	$\varepsilon_d'' - 2t_\varepsilon^\pi \left(\cos k_x a + \cos k_z a\right)$	0
$\|\boldsymbol{k}\ yz\rangle_\varepsilon$	0	0	$\varepsilon_d'' - 2t_\varepsilon^\pi \left(\cos k_y a + \cos k_z a\right)$

where the parameters in the matrix are

$$\varepsilon_d'' = \varepsilon_d + 4t_\varepsilon^\pi,$$

$$t_\varepsilon^\pi = \frac{|V_{pd\pi}|^2}{\varepsilon - \varepsilon_p}.$$

As in the case of the e_g bands, we find renormalized energy levels and effective band dispersions; since different Cu t_{2g} states couple to different F p states, and we neglected hopping integral between oxygens, the xy, xz, and yz bands are totally decoupled in our model. We are now in the position of calculating the (approximate) expression of the covalent contribution to the e_g-t_{2g} crystal-field splitting, i.e., the energy difference

$$\Delta_{\mathrm{CF}} \sim \varepsilon_d' - \varepsilon_d'' = 3\frac{|V_{pd\sigma}|^2}{\Delta_{pd}} - 4\frac{|V_{pd\pi}|^2}{\Delta_{pd}} > 0. \tag{13}$$

As we can see, the sign of the covalent crystal-field splitting is the same as that of the ionic contribution. This happens for two reasons. First, the so-called d bands are the anti-bonding states of the p-d Hamiltonian, hence both the energy of the e_g and t_{2g} states moves upwards due to the interaction with the p orbitals. Second, σ bonds are stronger than π bonds, hence e_g states shift to sizably higher energy than t_{2g} states.

The tight-binding model we have used so far is oversimplified, but it already qualitatively well describes the e_g and t_{2g} bands in Fig. 8. A more accurate description can be obtained including other Slater-Koster integrals, such as the hopping to apical F s states, or between neighboring F p states. With increasing number of parameters, it becomes progressively harder to estimate them, e.g., from comparison with experiments; furthermore a large number of fitting parameters makes it impossible to put a theory to a test. Modern techniques allow us, however, to calculate hopping integrals and crystal-field splittings *ab-initio*, using localized Wannier functions as basis instead of atomic orbitals, and the DFT potential $v_R(\boldsymbol{r})$ as one-electron potential; because Wannier functions are orthogonal, the corresponding overlap matrix is by construction diagonal.

4   Jahn-Teller effect

In order to introduce the Jahn-Teller effect we have to take a step backwards and start from the central equation of solid-state physics, the eigenvalue problem $\hat{H}\Psi = E\Psi$, defined (in the non-relativistic limit) by the many-body Hamiltonian

$$\hat{H} = \underbrace{-\frac{1}{2}\sum_i \nabla_i^2}_{\hat{T}_e} + \underbrace{\frac{1}{2}\sum_{i\neq i'}\frac{1}{|\boldsymbol{r}_i - \boldsymbol{r}_{i'}|}}_{\hat{V}_{ee}} - \underbrace{\sum_{i\alpha}\frac{Z_\alpha}{|\boldsymbol{r}_i - \boldsymbol{R}_\alpha|}}_{\hat{V}_{en}} - \underbrace{\sum_\alpha \frac{1}{2M_\alpha}\nabla_\alpha^2}_{\hat{T}_n} + \underbrace{\frac{1}{2}\sum_{\alpha\neq\alpha'}\frac{Z_\alpha Z_{\alpha'}}{|\boldsymbol{R}_\alpha - \boldsymbol{R}_{\alpha'}|}}_{\hat{V}_{nn}}.$$

Here $\{\boldsymbol{r}_i\}$ are the coordinates of the N_e electrons, $\{\boldsymbol{R}_\alpha\}$ those of the N_n nuclei, Z_α the atomic numbers, and M_α the nuclear masses. The Born-Oppenheimer Ansatz

$$\Psi(\{\boldsymbol{r}_i\}, \{\boldsymbol{R}_\alpha\}) = \psi(\{\boldsymbol{r}_i\}; \{\boldsymbol{R}_\alpha\})\, \Phi(\{\boldsymbol{R}_\alpha\})\,, \tag{14}$$

splits the Schrödinger equation $\hat{H}\Psi = E\Psi$ into the system

$$\begin{cases} \hat{H}_e \psi(\{\boldsymbol{r}_i\}; \{\boldsymbol{R}_\alpha\}) &= \varepsilon(\{\boldsymbol{R}_\alpha\})\psi(\{\boldsymbol{r}_i\}; \{\boldsymbol{R}_\alpha\}), \\[2mm] \hat{H}_n \Phi(\{\boldsymbol{R}_\alpha\}) &= E\Phi(\{\boldsymbol{R}_\alpha\}), \end{cases} \tag{15}$$

where the Hamilton operator for the electrons ($\hat{H}_e$) and that for the lattice ($\hat{H}_n$) are

$$\hat{H}_e = \hat{T}_e + \hat{V}_{ee} + \hat{V}_{en} + \hat{V}_{nn}, \tag{16}$$

$$\hat{H}_n = \hat{T}_n + \varepsilon(\{\boldsymbol{R}_\alpha\}) = \hat{T}_n + \hat{U}_n, \tag{17}$$

and where in (17) we neglect non-adiabatic corrections.[7] In the electronic Hamiltonian (16) the atomic positions $\{\boldsymbol{R}_\alpha\}$ are simple parameters. The electronic eigenvalue $\varepsilon(\{\boldsymbol{R}_\alpha\})$ acts as potential for the nuclei and defines a Born-Oppenheimer (BO) energy surface. While (16) describes the electronic structure, (17) yields the equilibrium crystal structure and the vibrational modes. These equations are impossible to solve in the general case. The first difficulty is that Hamiltonian (16) describes the electronic quantum many-body problem. The latter can be solved only approximately, for example the energy of the ground state can be obtained via density-functional theory using one of the known approximations to the universal functional. For strongly-correlated systems, advanced methods combine density-functional theory with many-body approaches such as the dynamical mean-field theory [7, 8]. The second issue is the very high number of atoms, and therefore of $\{\boldsymbol{R}_\alpha\}$ parameters to explore; finally, even if we solve the electronic many-body problem exactly, we still have to deal with the nuclear many-body problem, Hamiltonian (17). Despite all these obstacles, let us assume for a moment that, for a given system, we did solve the electronic problem for general values of $\{\boldsymbol{R}_\alpha\}$. Let us also assume that the set of positions $\{\boldsymbol{R}_\alpha\} = \{\boldsymbol{R}_\alpha^0\}$ defines a specific crystal structure, whose

---

[7]We neglect the operator $\hat{\Lambda}_n$, with elements $\langle m|\hat{\Lambda}_n|m'\rangle = -\sum_\alpha \frac{1}{M_\alpha}\left[\frac{1}{2}\langle\psi_m|\nabla_\alpha^2\psi_{m'}\rangle + \langle\psi_m|\nabla_\alpha\psi_{m'}\rangle\cdot\nabla_\alpha\right]$

electronic ground state (i.e., the lower energy BO surface) has degeneracy $d > 1$. We can at this point ask ourself the question: Is structure $\{R_\alpha^0\}$ actually stable?

The Jahn-Teller theorem states that any electronically degenerate system can lower its energy by undergoing some structural distortions, and therefore is unstable.[8] This is due to the coupling between electrons and lattice. In order to better understand the microscopic origin of this phenomenon, let us consider a system in a high-symmetry structure, $\{R_\alpha^0\}$, for which the electronic ground state has energy $\varepsilon(\{R_\alpha^0\})$ with degeneracy $d > 1$. This means that there are d Born-Oppenheimer surfaces degenerate for $\{R_\alpha\} = \{R_\alpha^0\}$,

$$\varepsilon_m(\{R_\alpha^0\}) = \varepsilon(\{R_\alpha^0\}).$$

In the rest of the chapter we will take $\varepsilon(\{R_\alpha^0\})$ as the energy zero. The corresponding degenerate electronic wavefunctions are $\psi_m(\{r_i\}; \{R_\alpha^0\})$. Let us expand the nuclear potential $\hat{U}_n$ for one of these surfaces around the symmetric structure $\{R_\alpha^0\}$. This leads to the Taylor series

$$\hat{H}_n = \hat{T}_n + \sum_{\alpha\mu} \left[\frac{\partial \hat{U}_n}{\partial u_{\alpha\mu}}\right]_{\{R_\alpha^0\}} u_{\alpha\mu} + \frac{1}{2}\sum_{\alpha\mu}\sum_{\alpha'\mu'} \left[\frac{\partial^2 \hat{U}_n}{\partial_{\alpha\mu}\partial_{\alpha'\mu'}}\right]_{\{R_\alpha^0\}} u_{\alpha\mu}\, u_{\alpha'\mu'} + \dots,$$

where $u_\alpha = R_\alpha - R_\alpha^0$ are displacement vectors with respect to the equilibrium position, and $\mu = x, y, z$. If $\{R_\alpha^0\}$ is an equilibrium structure, the gradient is zero and

$$\hat{H}_n \sim \hat{T}_n + \frac{1}{2}\sum_{\alpha\mu}\sum_{\alpha'\mu'} \left[\frac{\partial^2 \hat{U}_n}{\partial_{\alpha\mu}\partial_{\alpha'\mu'}}\right]_{\{R_\alpha^0\}} u_{\alpha\mu} u_{\alpha'\mu'} + \cdots = \hat{T}_n + \hat{U}_n^{\mathrm{PH}}(\{R_\alpha^0\}) + \dots, \quad (18)$$

The standard procedure to diagonalize (18) consists of two steps. First we change coordinates

$$\tilde{u}_{\alpha\mu} = u_{\alpha\mu}\sqrt{M_\alpha}.$$

Second we introduce the dynamical matrix

$$D_{\alpha\mu,\alpha\mu'} = \frac{1}{\sqrt{M_\alpha}}\frac{1}{\sqrt{M_{\alpha'}}} \left[\frac{\partial^2 \hat{U}_n}{\partial_{\alpha\mu}\partial_{\alpha'\mu'}}\right]_{\{R_\alpha^0\}},$$

and diagonalize it. Its N_m eigenvectors are the normal modes Q_η,

$$D Q_\eta = \omega_\eta^2 Q_\eta,$$

$$Q_{\eta\nu} = \sum_{\alpha=1}^{N_n}\sum_{\mu=x,y,z} a_{\eta\nu,\alpha\mu} u_{\alpha\mu},$$

with $\eta = 1, \dots N_m$, and $\nu = x, y, z$. The *normal coordinates* $\{Q_{n\nu}\}$, together with the associated canonically-conjugated momenta $\{P_{n\nu}\}$, bring (18) in the form

$$\hat{H}_n \sim \frac{1}{2}\sum_{\eta\nu} \left[P_{\eta\nu}^2 + \omega_\eta^2 Q_{\eta\nu}^2\right]. \quad (19)$$

---

[8] The only exceptions are linear molecules and Kramers degeneracy.

In a crystal, this Hamiltonian yields the phonon energy levels. Let us now determine the possible N_m normal modes for a cubic perovskite. For simplicity we consider here only a single octahedron and the modes associated with the vibrations of its atoms. Given that each atom can move in three directions, and there are 6 atoms of type C and 1 atom of type B, in principle such a system has 21 degrees of freedom; eliminating global translations (3 degrees of freedom) and global rotations (3 degrees of freedom), i.e., displacements which are not vibrations, 15 degrees of freedom are left, hence the system has 15 possible normal modes. In group theory language, assuming again for simplicity that the group is O instead of O_h, one can show that these modes can be labeled as belonging to irreducible representations A_1, E, T_1 or T_2. To obtain this result we first build a matrix representation of the group in the linear space of all possible displacements; this space is 21-dimensional, and so is the associated matrix representation Γ_{tot}. The latter can be expressed as the direct product $\Gamma_{\text{tot}} = \Gamma_{\text{a.s.}} \otimes \Gamma_{\text{vector}}$, where $\Gamma_{\text{a.s.}}$ is the so-called atomic-site representation. $\Gamma_{\text{a.s.}}$ has as a basis the original atomic positions (without displacements); in our case it is has therefore dimensionality 7. The character of $\Gamma_{\text{a.s.}}$ for a given operation is simply the number of sites left invariant by that operation. Finally, in group O the irreducible representation for a vector is $\Gamma_{vector} = T_1$; this can be seen from the partner functions (x, y, z) in Table 4. Summarizing all this in a character table, we have

O	E	$8C_3$	$3C_2$	$6C_2$	$6C_4$
$\Gamma^{\text{a.s.}}$	7	1	3	1	3
$\Gamma^{\text{tot}} = \Gamma^{\text{a.s.}} \otimes \Gamma_{\text{vector}}$	21	0	-3	-1	3

Once we know the characters for representation Γ_{tot}, we can split the latter into irreducible representations of group O via the decomposition formula Eq. (5). After subtracting (tensor subtraction $\ominus$) the representations for mere translations (T_1) and mere rotations (T_1) of the octahedron,[9] we arrive at the final decomposition of the vibrational-modes representation $\Gamma_{\text{vibrations}} = \Gamma_{\text{tot}} \ominus \Gamma_{\text{vector}} \ominus \Gamma_{\text{rotation}} = A_1 \oplus E \oplus 2T_1 \oplus 2T_2$. Normal modes which are a basis for different irreducible representations have in general different energies. Let us focus on modes A_1 and E. We can obtain mode A_1 by using the projector, Eq. (6), for irreducible representation A_1. As a matter of fact, if we assume that atom F_1 (Fig. 9) is displaced by $\boldsymbol{u}_1$, by applying the projector $\hat{P}^{A_1}$ to $\boldsymbol{u}_1$ we generate automatically the linear combination of atomic displacements (all having the same length) forming the mode of symmetry A_1. This leads to

$$\boldsymbol{Q}_0 = \boldsymbol{u}_1(q_0) + \boldsymbol{u}_2(q_0) + \boldsymbol{u}_3(q_0) + \boldsymbol{u}_4(q_0) + \boldsymbol{u}_5(q_0) + \boldsymbol{u}_6(q_0).$$

---

[9]The representation for an improper vector (rotation) is $\Gamma_{rotation} = T_1$, as can be seen from the corresponding partner functions (R_x, R_y, R_z) in Table 4.
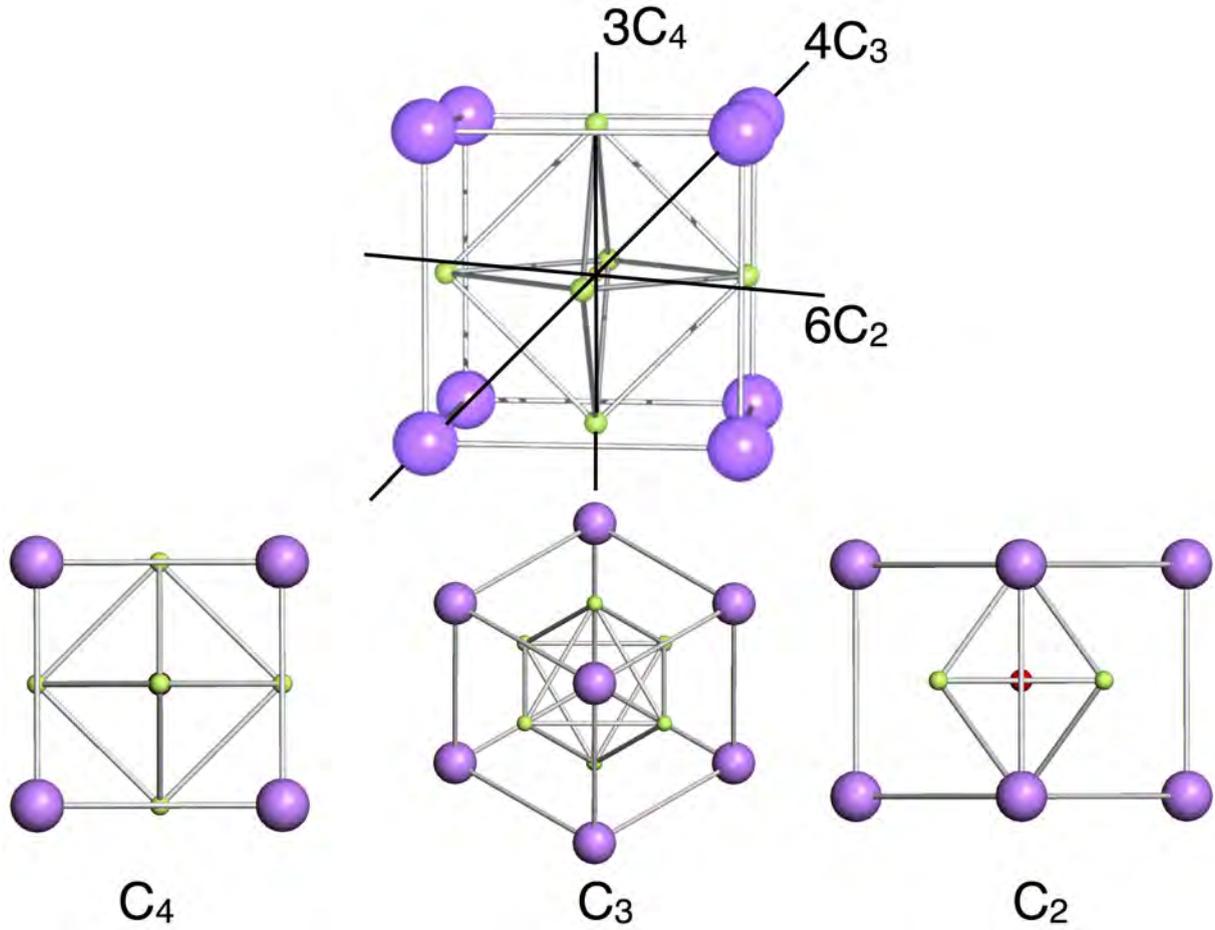
Fig. 9: *Unit cell (top) and vibrational modes Q_0, Q_1, and Q_2 of cubic KCuF$_3$.*

Here $\boldsymbol{u}_i$ are the (normalized) displacements for the C_i atom (see Fig. 9) which we rewrite as

$$
\begin{aligned}
\boldsymbol{u}_1(q_0) &= \tfrac{1}{\sqrt{6}} q_0 (1,0,0) \\
\boldsymbol{u}_2(q_0) &= \tfrac{1}{\sqrt{6}} q_0 (0,1,0) \\
\boldsymbol{u}_3(q_0) &= \tfrac{1}{\sqrt{6}} q_0 (0,0,1) \\
\boldsymbol{u}_4(q_0) &= -\tfrac{1}{\sqrt{6}} q_0 (1,0,0) \\
\boldsymbol{u}_5(q_0) &= -\tfrac{1}{\sqrt{6}} q_0 (0,1,0) \\
\boldsymbol{u}_6(q_0) &= -\tfrac{1}{\sqrt{6}} q_0 (0,0,1)
\end{aligned}
$$

The potential energy of such a *breathing mode* is

$$
U_n^{\mathrm{PH}} = \frac{1}{2} C_{A_1} q_0^2 \, .
$$

The $\boldsymbol{Q}_0$ mode expands or compresses the unit cell, but does not change its symmetry which remains cubic. Hence, this mode has no influence on the stability of the structure, at most it can affect the actual value of the lattice constant. More interesting are the two degenerate modes of type E. These modes can be obtained in a similar way as we have done for $\boldsymbol{Q}_0$, this time using the projector for irreducible representation E; within the resulting 2-dimensional space,

we choose as basis the mutually orthogonal modes that transform as the $l = 2$ partner functions of E, $x^2 - y^2$ and $3z^2 - r^2$. These are $\boldsymbol{Q}_1$ and $\boldsymbol{Q}_2$, shown in Fig. 9. They are defined as

$$\boldsymbol{Q}_1 = \boldsymbol{u}_1(q_1) + \boldsymbol{u}_2(q_1) + \boldsymbol{u}_4(q_1) + \boldsymbol{u}_5(q_1),$$

$$\boldsymbol{Q}_2 = \boldsymbol{u}_1(q_2) + \boldsymbol{u}_2(q_2) + \boldsymbol{u}_3(q_2) + \boldsymbol{u}_4(q_2) + \boldsymbol{u}_5(q_2) + \boldsymbol{u}_6(q_2),$$

where the displacements are

$$
\begin{array}{llll}
\boldsymbol{u}_1(q_1) & = & \frac{1}{\sqrt{4}}q_1(1,0,0) & \boldsymbol{u}_1(q_2) & = & -\frac{1}{\sqrt{12}}q_2(1,0,0) \\[4pt]
\boldsymbol{u}_2(q_1) & = & -\frac{1}{\sqrt{4}}q_1(0,1,0) & \boldsymbol{u}_2(q_2) & = & -\frac{1}{\sqrt{12}}q_2(0,1,0) \\[4pt]
\boldsymbol{u}_3(q_1) & = & (0,0,0) & \boldsymbol{u}_3(q_2) & = & \frac{2}{\sqrt{12}}q_2(0,0,1) \\[4pt]
\boldsymbol{u}_4(q_1) & = & -\frac{1}{\sqrt{4}}q_1(1,0,0) & \boldsymbol{u}_4(q_2) & = & \frac{1}{\sqrt{12}}q_2(1,0,0) \\[4pt]
\boldsymbol{u}_5(q_1) & = & \frac{1}{\sqrt{4}}q_1(0,1,0) & \boldsymbol{u}_5(q_2) & = & \frac{1}{\sqrt{12}}q_2(0,1,0) \\[4pt]
\boldsymbol{u}_6(q_1) & = & (0,0,0) & \boldsymbol{u}_6(q_2) & = & -\frac{2}{\sqrt{12}}q_2(0,0,1)
\end{array}
$$

The corresponding quadratic potential has the form

$$\hat{U}_n^{\mathrm{PH}} = \frac{1}{2}C_E(q_1^2 + q_2^2).$$

The normal modes T_1 and T_2 can be obtained in a similar way; since they are not relevant for structure stability in the example considered here we do not provide their form explicitly.

Up to now we have assumed that the hypothetical high-symmetry structure $\{\boldsymbol{R}_\alpha^0\}$ is a stationary point. In general, however, this might or might not be true. The behavior of the BO energy surfaces close to the point in which they are degenerate allows us to separate them into two classes, the first one in which $\{\boldsymbol{R}_\alpha^0\}$ is a stationary point for all degenerate electronic states m (Renner-Teller intersection), and the second in which the surface is not a stationary point at least for some of the surfaces (Jahn-Teller intersection). The classical Jahn-Teller systems are those for which $\nabla \hat{U}_n(\{\boldsymbol{R}_\alpha^0\}) \neq 0$ at least in some direction (see, e.g., Fig. 10). Let us now calculate the first-order correction to the m degenerate eigenvalues due to a small distortion around $\{\boldsymbol{R}_\alpha^0\}$. The electronic Hamiltonian (16) has matrix elements

$$\langle\psi_m|\hat{H}_e(\{\boldsymbol{R}_\alpha\})|\psi_{m'}\rangle = \underbrace{\sum_{\alpha\mu}\langle\psi_m|\left[\frac{\partial\hat{H}_e}{\partial u_{\alpha\mu}}\right]_{\{\boldsymbol{R}_\alpha^0\}}|\psi_{m'}\rangle u_{\alpha\mu}}_{\hat{U}_{m,m'}^{\mathrm{JT}}} + \cdots = \hat{U}_{m,m'}^{\mathrm{JT}} + \ldots.$$

The perturbation $\hat{U}^{\mathrm{JT}}$, the Jahn-Teller potential, couples the degenerate BO energy surfaces; it also couples electrons and lattice vibrations, as we can see from the coordinates $u_{\alpha\mu}$ appearing in the expression above. Thus, if there are modes for which $\hat{U}^{\mathrm{JT}} \neq C\hat{I}$ where $\hat{I}$ is the identity matrix and C a constant, the system gains energy at linear order via a distortion which lowers the symmetry; the Jahn-Teller theorem states that such modes always exist for electronically degenerate systems (with the exceptions of Kramers degeneracy and linear molecules).
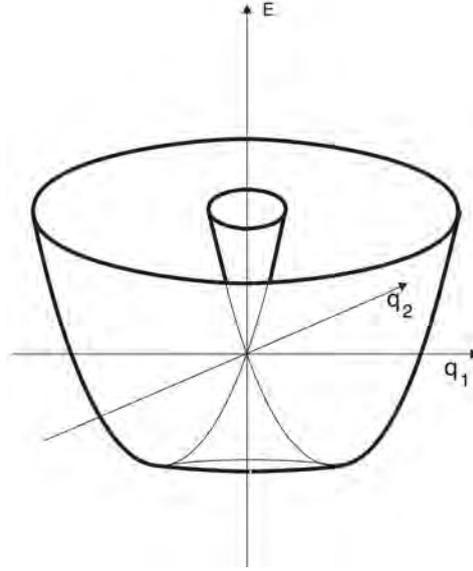
Fig. 10: *Born-Oppenheimer potential-energy surface exhibiting the form of a mexican hat. The slope of the curve at small distortions q_1, q_2 yields the Jahn-Teller coupling constant λ.*

In order to better understand the effect of the electron-lattice coupling, we generalize the Born-Oppenheimer Ansatz as follows

$$\Psi(\{\boldsymbol{r}_i\}, \{\boldsymbol{R}_\alpha\}) = \sum_m \psi_m(\{\boldsymbol{r}_i\}; \{\boldsymbol{R}_\alpha\}) \, \Phi_m(\{\boldsymbol{R}_\alpha\}).$$

To find the equations for the functions $\{\Phi_m\}$, we write the Schrödinger equation $H\Psi = E\Psi$, multiply on the left by $\overline{\psi_m}$, and integrate over the coordinates of the electrons. We obtain

$$\hat{H}_n \Phi_m(\{\boldsymbol{R}_\alpha\}) = \left[\hat{T}_n + \hat{U}_n^{\mathrm{PH}}\right] \Phi_m(\{\boldsymbol{R}_\alpha\}) + \sum_{m'} \hat{U}_{m,m'}^{\mathrm{JT}} \Phi_{m'}(\{\boldsymbol{R}_\alpha\}) = E\Phi_m(\{\boldsymbol{R}_\alpha\}). \quad (20)$$

The dynamics of the system close to the degeneracy point is determined by all degenerate sheets. The minimization of the new potential energy yields a new structure $\{\tilde{\boldsymbol{R}}_\alpha^0\}$ in which the electronic states are not any more degenerate. The modes that can produce such an instability should satisfy the condition

$$[\Gamma_m \otimes \Gamma_m] \cap \Gamma_{\mathrm{vibrations}} \supset A_1,$$

where Γ_m is the irreducible representation to which the electronic degenerate states belong, and $[\Gamma_m \otimes \Gamma_m]$ is the symmetric direct product. The trivial representation A_1 has to be excluded because, as already discussed, it does not lower the symmetry. In the case cubic $KCuF_3$ the relevant normal modes coupling to the degenerate e_g electronic states are the E modes; as for the electronic states, if the group $O \rightarrow O_h$, then $E \rightarrow E_g$. Thus we can say that $KCuF_3$ is an example of a $e_g \otimes E_g$ Jahn-Teller system, a system in which an electronic doublet (e_g) is coupled to a doublet of normal modes (E_g). The form of the Jahn-Teller potential $\hat{U}^{\mathrm{JT}}$ can be obtained from the effect of perturbations of type $\boldsymbol{Q}_1$ and $\boldsymbol{Q}_2$ on the crystal-field matrix. As for the crystal field, there are both a ionic and a covalent contribution. For the ionic contribution,

we can use once more perturbation theory. In this case, we have to take into account that the Cu-F distance d_C depends on the direction, i.e,

$$d_C \rightarrow d_C + \delta d_C^\mu,$$

where $\mu = x, y, z$; the specific δd_C^μ values for each atom are given by the specific vibrational mode. After summing up all contribution, the first non-cubic correction due to E_g modes is

$$\Delta v_{\mathrm{JT}} = \frac{q_C}{d_C^6} \frac{25}{14\sqrt{3}} \langle r^4 \rangle \begin{pmatrix} q_2 & q_1 \\ q_1 & -q_2 \end{pmatrix}.$$

It is, at this point, useful to introduce pseudo-spin operators acting on the e_g states, i.e., operators $\hat{\tau}_\mu$ with $\mu = x, y, z$ and

$$\hat{\tau}_z | \searrow \rangle = -| \searrow \rangle, \qquad \hat{\tau}_x | \searrow \rangle = +| \nearrow \rangle, \qquad \hat{\tau}_y | \searrow \rangle = -i| \nearrow \rangle$$

$$\hat{\tau}_z | \nearrow \rangle = +| \nearrow \rangle, \qquad \hat{\tau}_x | \nearrow \rangle = +| \searrow \rangle, \qquad \hat{\tau}_y | \nearrow \rangle = +i| \searrow \rangle$$

where $| \nearrow \rangle = |x^2 - y^2 \rangle$ and $| \searrow \rangle = |3z^2 - r^2 \rangle$. In matrix form these operators can be written as pseudo-Pauli matrices

$$\hat{\tau}_z = \begin{pmatrix} 1 & 0 \\ 0 & -1 \end{pmatrix} \quad \hat{\tau}_x = \begin{pmatrix} 0 & 1 \\ 1 & 0 \end{pmatrix} \quad \hat{\tau}_y = \begin{pmatrix} 0 & -i \\ i & 0 \end{pmatrix}. \tag{21}$$

We can then rewrite the Jahn-Teller potential as

$$\Delta v_{\mathrm{JT}} = \lambda \left[q_1 \tau_x + q_2 \tau_z \right],$$

where $\lambda = (q_C/d_C^6) (25/14\sqrt{3}) > 0$. This potential expresses both the essence of the Jahn-Teller theorem and its relation with orbital order; the systems gains energy at linear order by making a distortion; the latter produces a crystal-field splitting, which leads to preferential occupation of the lower energy level. For example, if $q_1 = 0$ and $q_2 < 0$ (tetragonal compression) the $3z^2 - r^2$ state is higher in energy. Let us now calculate the covalent contribution to the Jahn-Teller potential. In this case the linear-order correction is

$$\Delta \varepsilon_{lm,l'm'}(\mathbf{0}, \mathbf{R}_\alpha + \mathbf{u}) - \Delta \varepsilon_{lm,l'm'}(\mathbf{0}, \mathbf{R}_\alpha) \sim \nabla \Delta \varepsilon_{lm,l'm'}(\mathbf{0}, \mathbf{R}_\alpha) \cdot \mathbf{u}$$

For e_g-states we use for simplicity the following approximations[10]

$$\Delta \varepsilon_{3z^2 - r^2, 3z^2 - r^2} \sim \left[n^2 - \frac{1}{2}(l^2 + m^2) \right]^2 \tilde{V}_{dd\sigma},$$

$$\Delta \varepsilon_{3z^2 - r^2, x^2 - y^2} \sim \frac{\sqrt{3}}{2}(l^2 - m^2) \left[n^2 - \frac{1}{2}(l^2 + m^2) \right] \tilde{V}_{dd\sigma},$$

$$\Delta \varepsilon_{x^2 - y^2, x^2 - y^2} \sim \frac{3}{4}(l^2 - m^2)^2 \tilde{V}_{dd\sigma}.$$

---

[10]The crystal-field integrals are also two-center integrals; the table of Slater-Koster integrals in Appendix B is thus still valid, provided that $V_{ll'\alpha}$ are replaced by the corresponding crystal-field terms, which we indicate as $\tilde{V}_{ll'\alpha}$.
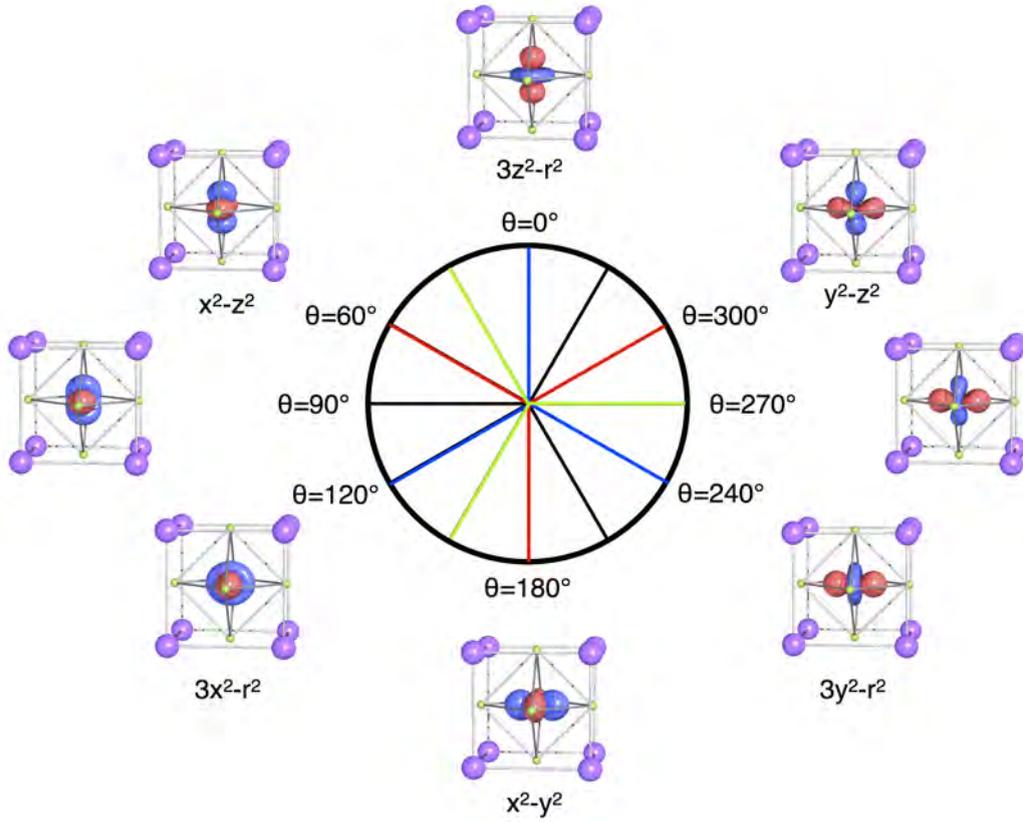
Fig. 11: *Linear combinations of e_g-states, $|\theta\rangle = -\sin\frac{\theta}{2}|x^2 - y^2\rangle + \cos\frac{\theta}{2}|3z^2 - r^2\rangle$. The $\theta = 0^o$ orbital is the excited state in the presence of a tetragonal compression along the z axis, while $\theta = \pm 2\pi/3$ are excited states for a tetragonal compression along x or y. This three-fold degeneracy (rotation by $\pm 2\pi/3$) is due to cubic symmetry.*

By summing up the contributions from all C ions for each mode, we obtain

$$\Delta\varepsilon_{\mathrm{JT}}(q_1, q_2) = \lambda \begin{pmatrix} q_2 & q_1 \\ q_1 & -q_2 \end{pmatrix} = \lambda\left[q_1\hat{\tau}_x + q_2\hat{\tau}_z\right],$$

where $\lambda \sim -\frac{\sqrt{3}}{2}\tilde{V}'_{dd\sigma} > 0$. This is the same form of potential that we have obtained for the ionic contribution. Again, if $q_1 = 0$ and $q_2 < 0$ (tetragonal compression) the $3z^2 - r^2$ is higher in energy. In conclusion, if we neglect the kinetic energy of the nuclei (limit $M_\alpha/m_e \to \infty$), the ground state of the system can be calculated by minimizing a potential energy of the form

$$\hat{U}(q_1, q_2) = \hat{U}^{\mathrm{JT}} + \hat{U}_n^{\mathrm{PH}} = \lambda \begin{pmatrix} q_2 & q_1 \\ q_1 & -q_2 \end{pmatrix} + \frac{1}{2}C_E\left(q_1^2 + q_2^2\right)\hat{I}, \qquad (22)$$

where $\hat{I}$ is the 2×2 identity matrix. To find the minimum of (22), it is convenient to introduce polar coordinates, which we define as $q_2 = -q\cos\theta$, $q_1 = -q\sin\theta$, so that for $0 < \theta < \pi/2$ we have $q_1 \leq 0$ (compression of $\hat{x}$ axis) and $q_2 \leq 0$ (compression of $\hat{z}$ axis); this corresponds to

the distortion of the octahedron labeled with number 1 in Fig. 1. In these coordinates

$$\hat{U}^{\mathrm{JT}} = -\lambda q \begin{pmatrix} \cos\theta & \sin\theta \\ \sin\theta & -\cos\theta \end{pmatrix}.$$

The diagonalization of matrix (22) yields two eigenvalues; the lower energy branch

$$E_-(q) = -\lambda q + \frac{C_E}{2}q^2$$

takes the form of a mexican hat, shown in Fig. 10. The minimum of $E_-(q)$ is obtained for $q = q_0 = \lambda/C$ and has value

$$E_{\mathrm{JT}} = -\lambda^2/2C_E;$$

the quantity E_{JT} is defined as the Jahn-Teller energy of the system. The electronic ground state can be written as

$$|\theta\rangle_G = -\sin\frac{\theta-\pi}{2}|x^2-y^2\rangle + \cos\frac{\theta-\pi}{2}|3z^2-r^2\rangle.$$

The excited state (hole orbital), with energy

$$E_+(q) = \lambda q + \frac{C_E}{2}q^2,$$

is then given by

$$|\theta\rangle_E = -\sin\frac{\theta}{2}|x^2-y^2\rangle + \cos\frac{\theta}{2}|3z^2-r^2\rangle.$$

The states $|\theta\rangle_E$ with different θ are shown in Fig. 11. In the simple model discussed so far, all states $|\theta\rangle_G$ have the same Jahn-Teller energy. Cubic symmetry, however, only requires that states

$$|\theta\rangle, \ |\theta+2\pi/3\rangle, \ |\theta-2\pi/3\rangle$$

are degenerate. The additional (accidental) degeneracy is removed when we take into account anharmonic terms, the lowest order of which has the form

$$U^{\mathrm{anh}}(q_1,q_2) = A(q_2^3 - 3q_2q_1^2) = Aq^3(\cos^3\theta - 3\cos\theta\sin^2\theta) = -Aq^3\cos 3\theta$$

and yields the tetragonal distortion as a ground state, with $\theta = 0, \pm 2\pi/3$ for positive A and with $\theta = \pi, \pi \pm 2\pi/3$ for negative A. Higher-order terms can make the $\boldsymbol{Q}_1$ Jahn-Teller distortion ($\theta = \pi/2, \pi/2 \pm 2\pi/3$) more stable [1]. For a periodic lattice, mode $\boldsymbol{Q}_1$ leads to a co-operative distortion where long and short bonds alternate in the x and y direction; in such a case, the hole orbital rotates by $\pi/2$ if we move from a Cu site to its Cu first-nearest neighbors in the $\boldsymbol{ab}$ plane. Let us now analyze the different electronic configurations that can occur in perovskites. For the electronic configuration $3d^1 = 3t_{2g}^1$, the procedure is as the one illustrated above, except that t_{2g} states are 3-fold degenerate and form π bonds, which are weaker, therefore the splitting introduced by the Jahn-Teller effect is smaller than for e_g states. In the case of electronic configurations $3d^n$ with $n > 1$, to determine if the ion is Jahn-Teller active one has to consider the degeneracies of the many-body state, including Coulomb repulsion. Weak Jahn-Teller states are $3d^1$ (Ti^{3+} in $\mathrm{LaTiO_3}$) and $3d^2$ (V^{3+} in $\mathrm{LaVO_3}$), as also $3t_{2g}^4, 3t_{2g}^5, 3t_{2g}^4e_g^2, 3t_{2g}^5e_g^2$; strong Jahn-Teller configurations are, e.g., $3d^9$ (Cu^{2+} in $\mathrm{KCuF_3}$) and $3t_{2g}^3e_g^1$ (Mn^{3+} in $\mathrm{LaMnO_3}$); the configurations $3t_{2g}^3$ and $3t_{2g}^3e_g^2$ are not degenerate and therefore not Jahn-Teller active.

5   Kugel-Khomskii superexchange

Let us now start from a totally different perspective, from the Hubbard model for a cubic per-ovskite with partially filled e_g shells. The Hamiltonian takes the form $\hat{H} = \hat{H}_0 + \hat{H}_T + \hat{H}_U$ where

$$\hat{H}_0 = \varepsilon_{e_g} \sum_i \sum_\sigma \sum_m \hat{n}_{im\sigma}$$

$$\hat{H}_T = -\sum_{i \neq i'} \sum_\sigma \sum_{mm'} t^{i,i'}_{mm'} c^\dagger_{im\sigma} c_{im'\sigma}$$

$$\hat{H}_U = U \sum_i \sum_m \hat{n}_{im\uparrow}\hat{n}_{im\downarrow} + \frac{1}{2}\sum_i \sum_{\sigma\sigma'} \sum_{m \neq m'} (U - 2J - J\delta_{\sigma,\sigma'})\, \hat{n}_{im\sigma}\hat{n}_{im'\sigma'}$$

$$-J \sum_i \sum_{m \neq m'} \left[c^\dagger_{im\uparrow} c^\dagger_{im\downarrow} c_{im'\uparrow} c_{im'\downarrow} + c^\dagger_{im\uparrow} c_{im\downarrow} c^\dagger_{im'\downarrow} c_{im'\uparrow} \right],$$

and where $m, m' = x^2 - y^2, 3z^2 - r^2$. Kugel and Khomskii have shown that, in the large t/U limit, this Hamiltonian can be mapped onto an effective generalized superexchange Hamiltonian with an orbitally-ordered ground state. To understand this, let us simplify the problem and consider first a system with only two atoms ($i = A, B$) for which the hopping matrix is diagonal in the orbitals

$$\hat{H}_T = -t \sum_\sigma \sum_m \left[c^\dagger_{Am} c_{Bm} + c^\dagger_{Bm} c_{Am} \right].$$

Furthermore, let us simplify the Coulomb interaction and neglect the spin-flip and pair-hopping terms

$$\hat{H}_U = U \sum_{i=AB} \sum_m \hat{n}_{im\uparrow}\hat{n}_{im\downarrow} + \frac{1}{2} \sum_{i=AB} \sum_{\sigma\sigma'} \sum_{m \neq m'} (U - 2J - J\delta_{\sigma,\sigma'})\, \hat{n}_{im\sigma}\hat{n}_{im'\sigma'}.$$

Finally, we assume that the systems has one electron per atom (quarter filling, e_g^1 configuration). In the $t = 0$ or atomic limit there are two types of possible states for this system, those in which each atom is occupied by one electron, $|1,1\rangle_\alpha$, and those in which one atom has two electrons and the other zero, $|2,0\rangle_{\alpha'}$. The 16 states of type $|1,1\rangle_\alpha$, all degenerate with energy $E_\alpha(1,1) = 2\varepsilon_{e_g}$, can be written as $c^\dagger_{Am_A\sigma_A} c^\dagger_{Bm_B\sigma_B}|0\rangle$ with $\alpha = (m_A\sigma_A, m_B\sigma_B)$; here $m_i\sigma_i$ are the quantum numbers for the electron at site $i = A, B$. There are 12 states $|2,0\rangle_\alpha$ with one atom occupied by two electrons; they are listed below together with their energies

$\lvert 2,0\rangle_{\alpha'}$			$E_{\alpha'}(2,0)$	
$\lvert 2,0\rangle_{i1m}$	$=$	$c^\dagger_{im\uparrow} c^\dagger_{im\downarrow}\lvert 0\rangle$	$2\varepsilon_{e_g} + U$	
$\lvert 2,0\rangle_{i2m}$	$=$	$c^\dagger_{im\uparrow} c^\dagger_{im'\downarrow}\lvert 0\rangle$	$2\varepsilon_{e_g} + U - 2J$	$m' \neq m$
$\lvert 2,0\rangle_{i3\sigma}$	$=$	$c^\dagger_{im\sigma} c^\dagger_{im'\sigma}\lvert 0\rangle$	$2\varepsilon_{e_g} + U - 3J$	$m' \neq m$

The Coulomb repulsion U is positive and J is small with respect to U; therefore the $|1,1\rangle_\alpha$ states define the ground-state manifold. If t is finite but small ($t/U \ll 1$), we can treat $\hat{H}_T$ as
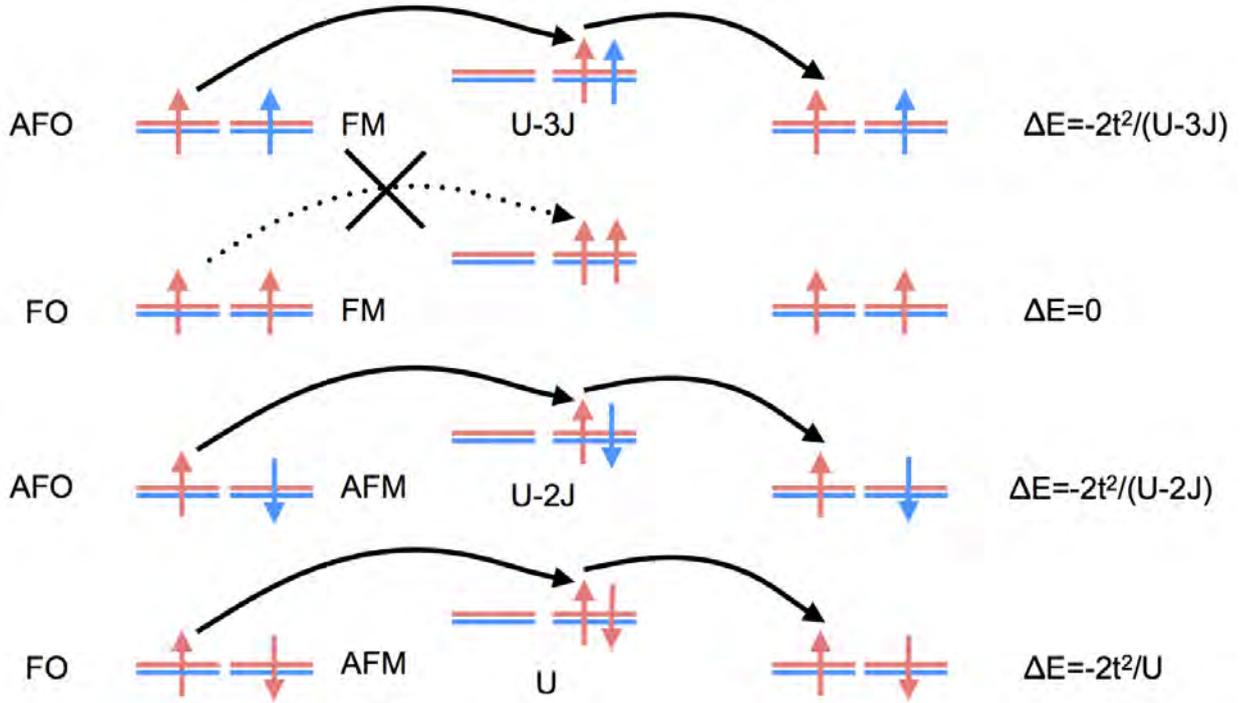
Fig. 12: *Superexchange energy gain for possible quarter-filling ground states of a two-site 2-fold degenerate Hubbard model with orbital- and spin-diagonal hopping matrices.*

a perturbation, and calculate the second-order correction to the energy of states $|1, 1\rangle_\alpha$. This correction is always negative (energy gain) and it is given by the matrix

$$\Delta E_{\alpha_1,\alpha_2}(1,1) = -\sum_{\alpha'} {}_{\alpha_1}\langle 1,1|\hat{H}_T|2,0\rangle_{\alpha'} \frac{1}{E_{\alpha'}(2,0) - E_\alpha(1,1)} {}_{\alpha'}\langle 2,0|\hat{H}_T|1,1\rangle_{\alpha_2}$$

There are four interesting cases, depicted in Fig. 12. The first is the ferro-magnetic (same spin) and antiferro-orbital (different orbitals) state, first line of the figure. The corresponding second order energy gain ($\alpha_1 = \alpha_2 = m\sigma, m'\sigma$) is

$$\Delta E_{\alpha_1,\alpha_1}(1,1) = -\frac{2t^2}{U - 3J}.$$

For the ferro-magnetic (same spin) and ferro-orbital (same orbital) state (second line in the figure, $\alpha_1 = \alpha_2 = m\sigma, m\sigma$) the energy gain is, instead, zero

$$\Delta E_{\alpha_1,\alpha_1}(1,1) = 0.$$

The reason is that no hopping is possible due to the Pauli principle. For the antiferro-magnetic antiferro-orbital state (third line, $\alpha_1 = \alpha_2 = m\sigma, m' - \sigma$), we have

$$\Delta E_{\alpha_1,\alpha_1}(1,1) = -\frac{2t^2}{U - 2J},$$

and finally for the antiferro-magnetic ferro-orbital state ($\alpha_1 = \alpha_2 = m\sigma, m - \sigma$) we find

$$\Delta E_{\alpha_1,\alpha_1}(1,1) = -\frac{2t^2}{U}.$$

Among these four states, the ferro-magnetic antiferro-orbital state is thus the lowest in energy. The main message is that the system gains superexchange energy by occupying preferentially different orbitals with the same spin, although the orbitals are by themselves degenerate. The 16×16 matrix of the second-order energy corrections $\Delta E_{\alpha_1,\alpha_2}(1,1)$ can be rewritten as the effective superexchange Hamiltonian

$$
\hat{H}_{\text{SE}} = 2\Gamma_{-+}\left[\boldsymbol{S}^A \cdot \boldsymbol{S}^B - \frac{1}{4}\right]\left[O_z^A\, O_z^B + \frac{1}{4}\right] + 2\Gamma_{+-}\left[\frac{1}{4} + S_z^A\, S_z^B\right]\left[\boldsymbol{O}^A \cdot \boldsymbol{O}^B - \frac{1}{4}\right]
$$
$$
+ 2\Gamma_{--}\left[\left(\boldsymbol{S}^A \cdot \boldsymbol{S}^B - S_z^A\, S_z^B\right)\left(\boldsymbol{O}^A \cdot \boldsymbol{O}^B - O_z^A\, O_z^B\right) - \left(S_z^A\, S_z^B - \frac{1}{4}\right)\left(O_z^A\, O_z^B - \frac{1}{4}\right)\right]
$$

where $\mathbf{O}_i = \boldsymbol{\tau}_i/2$ are operators acting only on orbital degrees of freedom and $\boldsymbol{\tau}$ are the pseudo-spin operators introduced in the previous section, Eq. (21), and

$$
\Gamma_{-+} = \frac{4t^2}{U} \qquad\qquad \Gamma_{+-} = \frac{4t^2}{U - 3J} \qquad\qquad \Gamma_{--} = -\frac{4t^2}{U - 2J}.
$$

When the second-order Hamiltonian is written in this form it is immediately clear that, among the four states we considered, the ferro-magnetic antiferro-orbital state is lower in energy. This happens because the superexchange coupling Γ_{+-} is the largest. If the orbital degeneracy is one, we can replace the terms $\boldsymbol{O}^A \cdot \boldsymbol{O}^B$ and $O_z^A\, O_z^B$ with the ferro-orbital value $1/4$; then, the terms proportional to Γ_{+-} and Γ_{--} drop out and we recover the Heisenberg superexchange Hamiltonian, as expected for the one-band Hubbard model.

What about KCuF$_3$ and LaMnO$_3$? If we consider only hopping integrals between neighboring B sites in the cubic perovskite structure, the hopping integral matrices take the simple form

$$
t_{mm'}^{i,i\pm\hat{z}} = t_\varepsilon \begin{pmatrix} 0 & 0 \\ 0 & 1 \end{pmatrix} \qquad t_{mm'}^{i,i\pm\hat{x}} = t_\varepsilon \begin{pmatrix} \frac{3}{4} & \frac{\sqrt{3}}{4} \\ \frac{\sqrt{3}}{4} & \frac{1}{4} \end{pmatrix} \qquad t_{mm'}^{i,i\pm\hat{y}} = t_\varepsilon \begin{pmatrix} \frac{3}{4} & -\frac{\sqrt{3}}{4} \\ -\frac{\sqrt{3}}{4} & \frac{1}{4} \end{pmatrix}. \tag{23}
$$

The structure of these matrices can be obtained by using Slater-Koster two-center integrals. The only non-zero hopping integral in the $\hat{z}$ direction is the one between $|3z^2 - r^2\rangle$ states. As we have previously seen by using the downfolding approach, it is given by $t_\varepsilon = V_{pd\sigma}^2/(\varepsilon - \varepsilon_p)$.

As in the case of the two-site molecule, for integer filling (n electrons per atom) and in the large t_ε/U limit the lattice Hubbard model can be mapped onto an effective superexchange Hamiltonian by downfolding high-energy states in which some of the atoms have an electron number larger than n. Only two electronic configurations are relevant for orbital ordering, e_g^1 (LaMnO$_3$) and e_g^3 (KCuF$_3$). The remaining partially filled state, e_g^2, is magnetic with $S = 1$ but, due to Hund's rule coupling J, it exhibits no orbital degeneracy ($L = 0$). After excluding e_g^2 we can, for simplicity, set $J = 0$. Let us now construct all atomic states $|N_e\rangle_\alpha$ with N_e electrons.

For a single atom they are

$|N_e\rangle_\alpha$	$E_{\alpha'}(N_e)$	$d(N_e)$
$|0\rangle$	$E(0) = 0$	$d(0) = 1$
$|1\rangle = c^\dagger_{m\sigma}|0\rangle$	$E(1) = \varepsilon_{e_g}$	$d(0) = 4$
$|2\rangle = c^\dagger_{m\sigma}c^\dagger_{m'\sigma'}|0\rangle$	$E(2) = 2\varepsilon_{e_g} + U$	$d(0) = 6$
$|3\rangle = c^\dagger_{m\sigma}c^\dagger_{m'\uparrow}c^\dagger_{m'\downarrow}|0\rangle$	$E(3) = 3\varepsilon_{e_g} + 3U$	$d(0) = 4$
$|4\rangle = c^\dagger_{m\uparrow}c^\dagger_{m\downarrow}c^\dagger_{m'\uparrow}c^\dagger_{m'\downarrow}|0\rangle$	$E(4) = 4\varepsilon_{e_g} + 6U$	$d(0) = 1$

The total (spin and orbital) degeneracy of the n-electron sector, $d(N_e)$, is given in the third column. Let us consider two neighboring sites i and i' and their states $|N_e\rangle^i_\alpha$ and $|N'_e\rangle^{i'}_{\alpha'}$, where α and α' run over all degenerate states in the N_e-electron sector. We define the collective state of such a two-site system as $|N_e\rangle^i_\alpha|N'_e\rangle^{i'}_{\alpha'}$. Let us start from an e^1_g configuration. In the large-U limit, at quarter filling ($n = 1$) the ground state will be within the $N_e = N'_e = 1$ manifold, $|G\rangle = \{|1\rangle^i_\alpha|1\rangle^{i'}_{\alpha'}\}$. The latter has a degeneracy 4^N, where N is the number of sites, here $N = 2$; this degeneracy can be partially lifted via virtual excitations to the doubly occupied states $|E\rangle = \{|2\rangle^i_\alpha|0\rangle^{i'}\}, \{|0\rangle^i|2\rangle^{i'}_{\alpha'}\}$, which in turn generate an effective low-energy Hamiltonian $\hat{H}_{SE}$. We can again calculate $\hat{H}_{SE}$ by treating $\hat{H}_T$ as a perturbation.

Let us consider at first only pairs of sites along the $\hat{z}$ axis. In second-order perturbation theory in $\hat{H}_T$, we obtain for the lattice the following effective Hamiltonian

$$\hat{H}^{\hat{z}}_{SE} \sim -\frac{1}{U}\sum_E \hat{H}_T|E\rangle\langle E|\hat{H}^\dagger_T$$

$$= -\frac{t^2}{U}\frac{1}{2}\sum_{ii'}\sum_{\sigma\sigma'}\sum_\alpha \left\{ c^\dagger_{i\tau\sigma}|0\rangle^{i\ i}\langle 0|c_{i\tau\sigma'}\left[c_{i'\tau\sigma}|2\rangle^{i'\ i'}_{\alpha\ \alpha}\langle 2|c^\dagger_{i'\tau\sigma'}\right] + (i \longleftrightarrow i') \right\}\delta_{\tau,\searrow}$$

$$= -\frac{2t^2}{U}\frac{1}{2}\sum_{ii'}\sum_{\sigma\sigma'}\left\{ (-1)^{-\sigma'-\sigma}P^i_{\tau\sigma-\sigma'}P^{i'}_{\tau\sigma'-\sigma} + \frac{1}{2}\left[P^i_{\tau\sigma\sigma}P^{i'}_{-\tau\sigma'\sigma'} + P^i_{-\tau\sigma\sigma}P^{i'}_{\tau\sigma'\sigma'}\right] \right\}\delta_{\tau,\searrow},$$

where we already replaced in the denominator $\Delta E = E(2) + E(0) - 2E(1)$ with its value, U, and where, once more, $|\searrow\rangle = |3z^2 - r^2\rangle$, $|\nearrow\rangle = |x^2 - y^2\rangle$. In Hamiltonian $\hat{H}^{\hat{z}}_{SE}$ we introduced the operators $P^i_{\tau\sigma\sigma'}$, which are given by

$$P^i_{\tau\sigma\sigma'} = c^\dagger_{i\tau\sigma}|0\rangle\langle 0|c_{i\tau\sigma'} = \hat{o}^z_{\tau\tau}\left[\hat{s}^z_{\sigma\sigma'} + \hat{s}^+_{\sigma\sigma'} + \hat{s}^-_{\sigma\sigma'}\right].$$

In this expression on the right-hand side we rewrote $P^i_{\tau\sigma\sigma'}$ as product of an orbital and a spin term, defined as follows:

$$\hat{o}^z_{\tau\tau'} = \left[\frac{n_i}{2}\hat{I} + (-1)^\tau O^i_z\right]\delta_{\tau\tau'} \qquad\qquad \hat{s}^z_{\sigma\sigma} = \left[\frac{n_i}{2}\hat{I} + (-1)^\sigma S^i_z\right]\delta_{\sigma\sigma'}$$

$$\hat{o}^+_{\tau\tau'} = O^i_+(1 - \delta_{\tau\tau'}) \qquad\qquad \hat{s}^+_{\sigma\sigma'} = S^i_+(1 - \delta_{\sigma\sigma'})$$

$$\hat{o}^-_{\tau\tau'} = O^i_-(1 - \delta_{\tau\tau'}) \qquad\qquad \hat{s}^-_{\sigma\sigma'} = S^i_-(1 - \delta_{\sigma\sigma'}),$$

where $(-1)^\sigma = +1$ for spin (pseudospin) up and -1 otherwise; the operator $\hat{I}$ is the identity matrix. Hence, we can express the effective Hamiltonian as

$$\hat{H}_{\mathrm{SE}}^{\hat{z}} = \frac{\Gamma}{2} \sum_{ii'} \left[\boldsymbol{S}^i \cdot \boldsymbol{S}^{i'} - \frac{n_i n_{i'}}{4} \right] \left[O_z^i - \frac{n_i}{2} \right] \left[O_z^{i'} - \frac{n_{i'}}{2} \right] + \frac{1}{2} \left[O_z^i O_z^{i'} - \frac{n_i n_{i'}}{4} \right],$$

where $\Gamma = 4t^2/U > 0$. If we drop all processes involving orbital $| \nearrow \rangle$ we recover the usual superexchange Heisenberg Hamiltonian for the one-band Hubbard model

$$\hat{H}_{\mathrm{SE}}^{\hat{z}} = \frac{\Gamma}{2} \sum_{ii'} \left[\boldsymbol{S}^i \cdot \boldsymbol{S}^{i'} - \frac{n_i n_{i'}}{4} \right].$$

Let us now consider two neighboring sites and the energy of some possible states $|G\rangle = \{ |1\rangle_\alpha^i |1\rangle_{\alpha'}^{i'} \}$. A ferro-magnetic spin configuration has energy

$$\Delta E_{\tau\uparrow,\tau'\uparrow} = -\frac{\Gamma}{4}(1 - \delta_{\tau,\tau'}),$$

hence, there is an energy gain if the electrons occupy different orbitals, i.e., if the systems has antiferro-orbital arrangement. Let us consider now a antiferro-magnetic spin arrangement. The corresponding energy is

$$\Delta E_{\tau\uparrow,\tau'\downarrow} = -\frac{\Gamma}{2}\delta_{\tau,\tau'}\delta_{\tau,\searrow} - \frac{\Gamma}{4}(1 - \delta_{\tau,\tau'})$$

The expression above shows that in the antiferro-magnetic case the system gains more energy if the occupied state is $| \searrow \rangle$ at both sites. Up to now we considered magnetically ordered states. In LaMnO$_3$ and KCuF$_3$, however, orbital order takes place well above the magnetic transition. Let us then assume that the system is orbitally ordered but paramagnetic, with occupied state

$$|\theta\rangle_i = -\sin\frac{\theta - \pi}{2}|x^2 - y^2\rangle + \cos\frac{\theta - \pi}{2}|3z^2 - r^2\rangle$$

at site i and $|\theta\rangle_{i\pm\hat{z}} = |\theta\rangle_i$ at the neighboring site $i' = i \pm \hat{z}$. This choice corresponds to ferro-orbital order along $\hat{z}$, the type of stacking realized in LaMnO$_3$ (see Fig. 13). What is the value of θ than minimizes the energy? We can calculate it using the variational method. The superexchange energy gain with respect to a paramagnetic paraorbital state is given by

$$\Delta E(\theta) = \frac{\Gamma}{16} \left[\cos^2(\theta - \pi) + 2\cos(\theta - \pi) \right].$$

This function is minimized for $\theta = 0$, an angle corresponding to a tetragonal compression. To determine the optimal angle for the three-dimensional system we have in addition to take into account the effective Hamiltonian stemming from virtual hoppings in the remaining directions. Due to cubic symmetry, if we rotate the quantization axis, the superexchange Hamiltonian has the same form in all directions; to sum up all terms we have merely to rotate back the quantization axis to $\hat{z}$. Hence, we have to make the replacements

$$O_z^i \underset{\hat{z}\to\hat{x}}{\longrightarrow} -\frac{1}{2}O_z^i - \frac{\sqrt{3}}{2}O_x^i$$

$$O_z^i \underset{\hat{z}\to\hat{y}}{\longrightarrow} -\frac{1}{2}O_z^i + \frac{\sqrt{3}}{2}O_x^i$$

Fig. 13: *Orbital order (LDA+DMFT calculations) in the rare-earth perovskite TbMnO$_3$ with the GdFeO$_3$-type structure. From Ref. [6]. This system has the same structure of LaMnO$_3$.*

Let us assume antiferro-orbital order in the plane, again as in the case of LaMnO$_3$, shown in Fig. 13. This means that, for $i' = i \pm \hat{x}$ or $i' = i \pm \hat{y}$, the occupied state is

$$|\theta\rangle_{i'} = + \sin\frac{\theta - \pi}{2}|x^2 - y^2\rangle + \cos\frac{\theta - \pi}{2}|3z^2 - r^2\rangle.$$

We can easily verify that $|\theta\rangle_{i'} = |-\theta + 2\pi\rangle_i$. This is state $|\theta\rangle_i$ rotated by $\pi/2$ ($x \to y$, $y \to -x$). The total superexchange energy gain with respect to a paramagnetic paraorbital state is then given by

$$\Delta E(\theta) = \frac{\Gamma}{16}\left[3\cos^2(\theta - \pi) - \frac{3}{2}\right].$$

This expression has a minimum for $\theta = \pi/2$ (Jahn-Teller-like $\boldsymbol{Q}_1$ distortion). For the e_g^3 configuration (KCuF$_3$), due to particle-hole symmetry, we obtain the same result. This can be verified by observing, first of all, that the e_g bands obtained from the hopping-integrals matrices (23) – bands which we have discussed in detail in Sec. 3 – are symmetric with respect to the Fermi level for half filling. In addition, the energy difference entering in the denominator of the superexchange Hamiltonian for an e_g^3 ground state, $\Delta E = E(4) + E(2) - 2E(3)$, has the same value ($\Delta E = U$) as in the case of an e_g^1 ground state. The main difference between LaMnO$_3$ (e_g^1) and KCuF$_3$ (e_g^3), for what concerns the results presented in this section, is that the stacking along $\hat{z}$, ferro-orbital for LaMnO$_3$, can be either antiferro- or ferro-orbital for KCuF$_3$; Fig. 1 shows the case of antiferro-orbital arrangement. Remarkably, the variational energy gain $\Delta E(\theta)$ is the same for both types of stacking along $\hat{z}$, i.e., for $|\theta\rangle_{i \pm \hat{z}} = |\theta\rangle_i$ and for $|\theta\rangle_{i \pm \hat{z}} = |-\theta + 2\pi\rangle_i$. The conclusions of this section are thus identical for LaMnO$_3$ and KCuF$_3$.
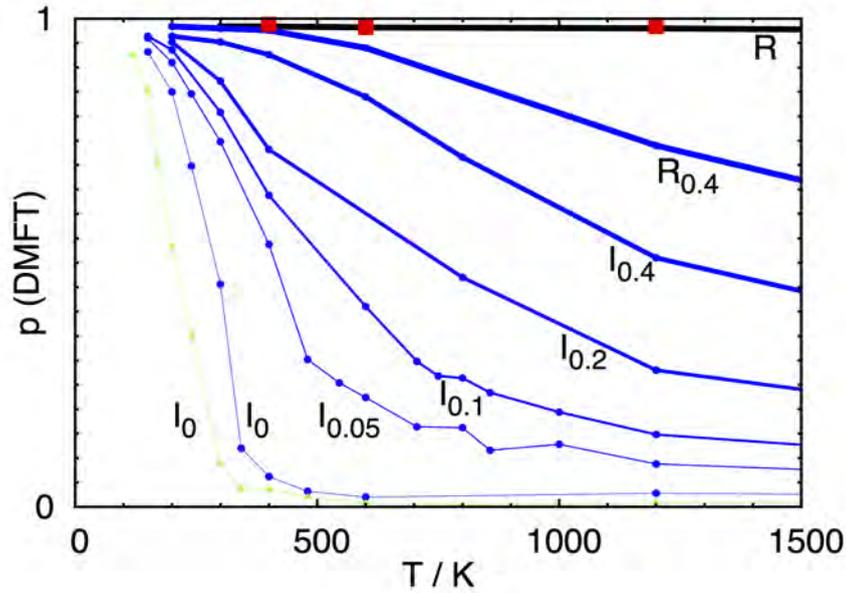
Fig. 14: *Orbital order transition in KCuF$_3$. Orbital polarization p as a function of temperature calculated in LDA+DMFT. R: experimental structure. Circles: idealized structures R_δ and I_δ with decreasing crystal-field and $U = 7$ eV. Green/Triangles: $U = 9$ eV, I_0 only. Red/Squares: two-sites CDMFT. From Ref. [3].*

6 The origin of orbital order

As we discussed in the introduction, the hallmark of orbital order is the co-operative Jahn-Teller distortion. This static distortion gives rise to a crystal field, which splits the otherwise degenerate e_g doublet. Due to Coulomb repulsion, it turns out that even a crystal-field splitting much smaller than the band width can lead to orbital order. The importance of this effect for real materials has been realized first for LaTiO$_3$ and YTiO$_3$ [4]. This reduction of orbital fluctuation is dynamical, but it can be already understood from the static Hartree-Fock contribution to the self-energy; the latter yields an effective enhancement of the crystal-field proportional to orbital polarization p. For an e_g system p is defined as the difference in occupation between the most and the least occupied orbital, $|1\rangle$ and $|2\rangle$, the so-called natural orbitals. Thus $p = n_1 - n_2$, and the Hartree-Fock self-energy correction to the crystal-field splitting is

$$\Delta\varepsilon_{\mathrm{CF}} = \Sigma_2(\omega_n \to \infty) - \Sigma_1(\omega_n \to \infty) \sim \frac{1}{2}(U - 5J)p.$$

If $p > 0$, as it happens in the presence of a crystal-field $\varepsilon_{\mathrm{CF}} = \varepsilon_2 - \varepsilon_1 > 0$, this term effectively increases the crystal-field splitting. This effect is at work not only in LaTiO$_3$ and YTiO$_3$, but also in several other systems with different electronic structure and even smaller crystal-field splittings. The case of $3d^9$ KCuF$_3$ and $3d^4$ LaMnO$_3$ is extreme: the e_g crystal-field splitting is $\sim 0.5 - 1$ eV; with such a large splitting, orbital fluctuations are suppressed up to the melting temperature. Thus, Coulomb repulsion makes the Jahn-Teller mechanism proposed by Kanamori very efficient. This result, however, does not clarify which of the two mechanisms,
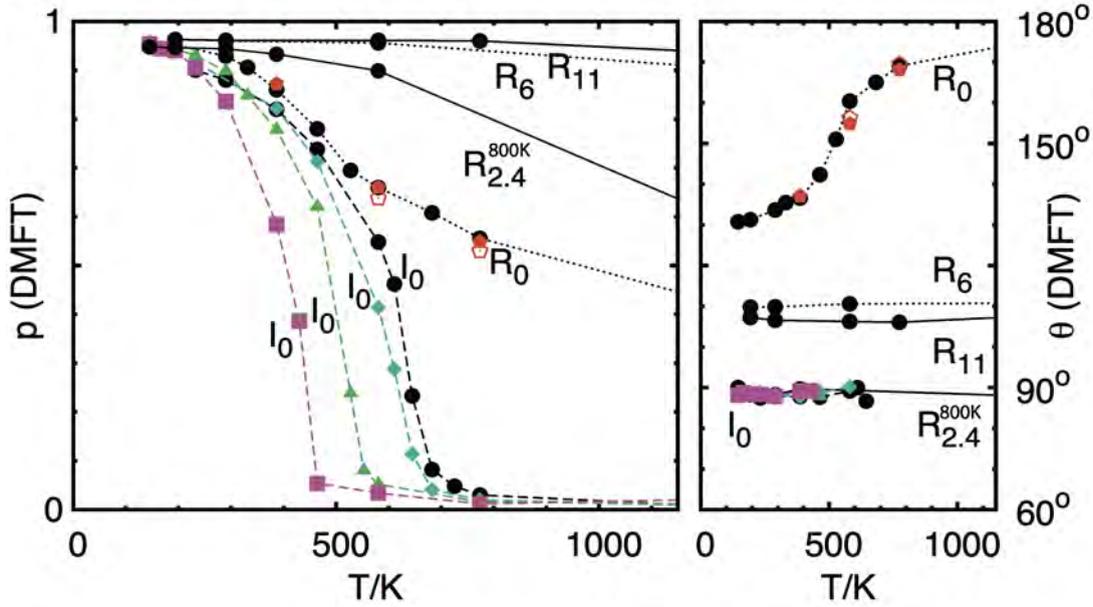
Fig. 15: *Orbital order transition in LaMnO$_3$. Orbital polarization p (left) and (right) occupied state $|\theta\rangle = \cos\frac{\theta}{2}|3z^2 - r^2\rangle + \sin\frac{\theta}{2}|x^2 - y^2\rangle$ as a function of temperature. Solid lines: 300 K experimental structure (R_{11}) and 800 K experimental structure. Dots: orthorhombic structures with half (R_6) or no (R_0) Jahn-Teller distortion. Pentagons: 2 (full) and 4 (empty) site CDMFT. Dashes: ideal cubic structure (I_0). Circles: $U = 5$ eV. Diamonds: $U = 5.5$ eV. Triangles: $U = 6$ eV. Squares: $U = 7$ eV. Crystal field splittings (meV): 840 (R_{11}), 495 (R_6), 168 ($R_{2.4}^{800\,K}$), and 0 (I_0). From Ref. [6].*

Kugel-Khomskii superexchange or Kanamori electron-phonon coupling, plays the major role in causing orbital order and stabilizing the distortion. Remarkably, Coulomb repulsion has also an important effect on structure stabilization. LDA+U total energy calculations have early on shown that the co-operative Jahn-Teller distortion is stabilized by U [10, 11], a result confirmed recently by LDA+DMFT [12]. This could be – and initially was – taken as an indication that superexchange is the driving mechanism. If this is the case, it is, however, hard to explain why the magnetic transition temperature ($T_N \sim 40$ K for KCuF$_3$ and $T_N \sim 140$ K for LaMnO$_3$), also determined by superexchange, is relatively low while the co-operative Jahn-Teller distortion persists up to the melting temperature. On the other hand, if Kugel-Khomskii superexchange is not the driving mechanism, the associated energy gain should be small with respect to the total energy gain due to the Jahn-Teller distortion.

To clarify the nature of the dominant mechanism, we disentangled electron-phonon and superexchange effects. To this end we performed LDA+DMFT (single-site and cluster) calculations for a series of hypothetical structures, in which the distortions (and thus the crystal-field splitting) are progressively reduced. In the case of KCuF$_3$, these hypothetical structures are shown in Fig. 1, and the corresponding e_g bands are shown in Fig. 7. For each structure we calculate the order parameter, the orbital polarization p. In Fig. 14 we show p as a function of temperature. For the experimental structure (R in the figure), we find that $p(T) \sim 1$ up to the melting temperature. The empty orbitals on different sites make the pattern shown in Fig. 1. For
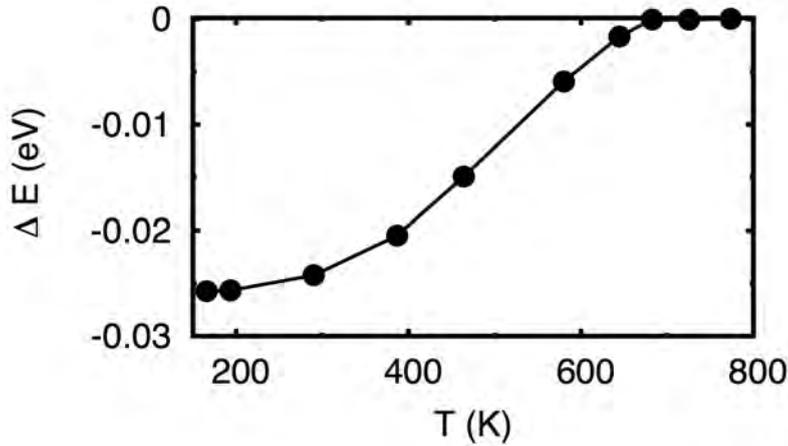
Fig. 16: *Superexchange energy gain for LaMnO$_3$, $\Delta E \sim -T_{\mathrm{KK}}/2$. From Ref. [6].*

the ideal cubic structure I_0, we find that $p(T) = 0$ at high temperature, but a transition occurs at $T_{\mathrm{KK}} \sim 350$ K. This T_{KK} is the critical temperature in the absence of electron-phonon coupling, i.e., the superexchange critical temperature. Our results show that around 350 K superexchange alone could indeed drive the co-operative Jahn-Teller distortion; it cannot, however, explain the presence of a co-operative Jahn-Teller distortion above 350 K. We performed a similar study fo LaMnO$_3$. For this $t_{2g}^3 e_g^1$ system we have to take into account the Hund's rule coupling between e_g electrons and t_{2g} spins, $\boldsymbol{S}_{t_{2g}}$. Thus the minimal model to understand orbital order is the modified Hubbard model [13]

$$H = -\sum_{ii'}\sum_{\sigma\sigma'}\sum_{mm'} t_{m,m'}^{i,i'}\, u_{\sigma,\sigma'}^{i,i'}\, c_{im\sigma}^\dagger c_{i'm'\sigma'} - h \sum_{im}(\hat{n}_{im\uparrow} - \hat{n}_{im\downarrow})$$

$$+ U \sum_{im}\hat{n}_{im\uparrow}\hat{n}_{im\downarrow} + \frac{1}{2}\sum_i\sum_{\sigma\sigma'}\sum_{m(\neq m')} (U - 2J - J\delta_{\sigma,\sigma'})\,\hat{n}_{im\sigma}\hat{n}_{im'\sigma'}\ .$$

Here the local magnetic field $h = JS_{t_{2g}}$ describes the Hund's rule coupling to t_{2g} electrons, and $u_{i\sigma,i'\sigma'} = 2/3(1 - \delta_{i,i'})$ accounts for the disorder in orientation of the t_{2g} spins. By performing the same type of analysis as for KCuF$_3$, we find the impressively large $T_{\mathrm{KK}} \sim 700$ K (Fig. 15). There is a small point neglected so far; besides the co-operative Jahn-Teller distortion and tetragonal compression, LaMnO$_3$ exhibits a GdFeO$_3$-type distortion (Fig. 13), which tends to reduce the e_g band width [4]. To account for this we studied the orbital-order transition for the ideal structure R_0, which retains all distortions except for the Jahn-Teller one. For structure R_0 we cannot obtain T_{KK} from $p(T)$, because, due to the ~ 200 meV crystal-field splitting, Coulomb repulsion strongly suppress orbital fluctuations even at 1500 K. We can, however, study the evolution with temperature of the occupied orbital, here defined as $|\theta\rangle = \cos\frac{\theta}{2}|3z^2 - r^2\rangle + \sin\frac{\theta}{2}|x^2 - y^2\rangle$. For the experimental structure (R_{11}) we find $\theta \sim 108^o$, in agreement with experiments, while for the I_0 structure we obtain $\theta = 90^o$. For the R_0 structure we find two regimes: At high temperature the occupied orbital is the lower-energy crystal-field orbital ($\theta = 180^o$). At $T_{\mathrm{KK}} \sim 550$ K superexchange rotates this θ towards 90°, reaching

130^0 in the zero-temperature limit; this is the actual superexchange transition temperature for LaMnO$_3$. Such T_{KK} is still remarkably large, however not sufficiently to explain the persistence of the Jahn-Teller distortion in nanoclusters up to basically melting temperature [14]. Furthermore, the superexchange energy gain associated with orbital order (Fig.16) is small compared to the total energy gain due to the Jahn-Teller distortion, calculated via LDA+U [10, 11] or LDA+DMFT [12]. Thus, as in the case of KCuF$_3$, the conclusion is that a static crystal-field splitting, as the one generated by the electron-lattice coupling, is essential to explain orbital ordering at high temperature.

7   Conclusion

In this lecture we have studied two mechanisms that can lead to orbital ordering phenomena in Mott insulators. The first one is well illustrated in the influential paper of Kanamori, Ref. [1]. In this picture, a co-operative Jahn-Teller distortion generates a static crystal-field, which in turn splits orbitals otherwise degenerate. This mechanism is made more efficient by Coulomb repulsion; the latter enhances the orbital polarization, leading to a orbitally-ordered state even if the crystal-field splitting is a mere fraction of the bandwidth [4]. The second mechanism, proposed by Kugel and Khomskii [2] in 1973, predicts orbital ordering even in the absence of a static crystal field; in this picture, orbital ordering is due to the superexchange interaction, the effective interaction emerging from the orbitally-degenerate Hubbard model in the large U limit. Since both mechanism predict a similar type of order, identifying which one dominates for real materials is very difficult. Indeed, the origin of orbital order has been a matter of debate for decades. In the last section we saw how this problem was recently solved by disentangling the superexchange Kugel-Khomskii interaction from the rest. It was shown for the two most representative orbitally-ordered materials, KCuF$_3$ and LaMnO$_3$, that although Kugel-Khomskii superexchange is very efficient, it cannot alone explain the presence of a co-operative Jahn-Teller distortion up to the melting temperature. An interaction giving directly rise to a crystal-field splitting, e.g., electron-phonon coupling, is necessary to explain experimental findings.

Acknowledgment

Appendices

A Constants and units

In this lecture, formulas are given in atomic units. The unit of mass m_0 is the electron mass ($m_0 = m_e$), the unit of charge e_0 is the electron charge ($e_0 = e$), the unit of length a_0 is the Bohr radius ($a_0 = a_B \sim 0.52918$ Å), and the unit of time is $t_0 = 4\pi\varepsilon_0\hbar a_0/e^2$. In these units, m_e, a_B, e and $1/4\pi\varepsilon_0$ have the numerical value 1, the speed of light is $c = 1/\alpha \sim 137$, and the unit of energy is $1\mathrm{Ha} = e^2/4\pi\varepsilon_0 a_0 \sim 27.211$ eV.

B Atomic orbitals

B.1 Radial functions

The nlm hydrogen-like atomic orbital is given by

$$\psi_{nlm}(\rho, \theta, \phi) = R_{nl}(\rho)Y_l^m(\theta, \phi),$$

where $R_{nl}(\rho)$ is the radial function and $Y_m^l(\theta, \phi)$ a spherical harmonic, $\rho = Zr$ and Z the atomic number. In atomic units, the radial functions are

$$R_{nl}(\rho) = \sqrt{\left(\frac{2Z}{n}\right)^3 \frac{(n-l-1)!}{2n[(n+l)!]^3}} e^{-\rho/n} \left(\frac{2\rho}{n}\right)^l L_{n-l-1}^{2l+1}\left(\frac{2\rho}{n}\right),$$

where L_{n-l-1}^{2l+1} are generalized Laguerre polynomials of degree $n - l - 1$.
The radial function for $n = 1, 2, 3$ are

$$
\begin{array}{rlll}
R_{1s}(\rho) = & 2 & Z^{3/2} & e^{-\rho} \\
R_{2s}(\rho) = & \frac{1}{2\sqrt{2}} & Z^{3/2} & (2-\rho)\, e^{-\rho/2} \\
R_{2p}(\rho) = & \frac{1}{2\sqrt{6}} & Z^{3/2} & \rho\, e^{-\rho/2} \\
R_{3s}(\rho) = & \frac{2}{3\sqrt{3}} & Z^{3/2} & (1 - 2\rho/3 + 2\rho^2/27)\, e^{-\rho/3} \\
R_{3p}(\rho) = & \frac{4\sqrt{2}}{9\sqrt{3}} & Z^{3/2} & \rho(1 - \rho/6)\, e^{-\rho/3} \\
R_{3d}(\rho) = & \frac{2\sqrt{2}}{81\sqrt{15}} & Z^{3/2} & \rho^2\, e^{-\rho/3}
\end{array}
$$

where we used the standard notation s for $l = 0$, p for $l = 1$ and d for $l = 2$.

B.2 Real harmonics

To study solids, it is usually convenient to work in the basis of real harmonics. The latter are defined in terms of the spherical harmonics as follows:

$$y_{l0} = Y_0^l, \quad y_{lm} = \frac{1}{\sqrt{2}}(Y_{-m}^l + (-1)^m Y_m^l), \quad y_{l-m} = \frac{i}{\sqrt{2}}(Y_{-m}^l - (-1)^m Y_m^l), \quad m > 0.$$
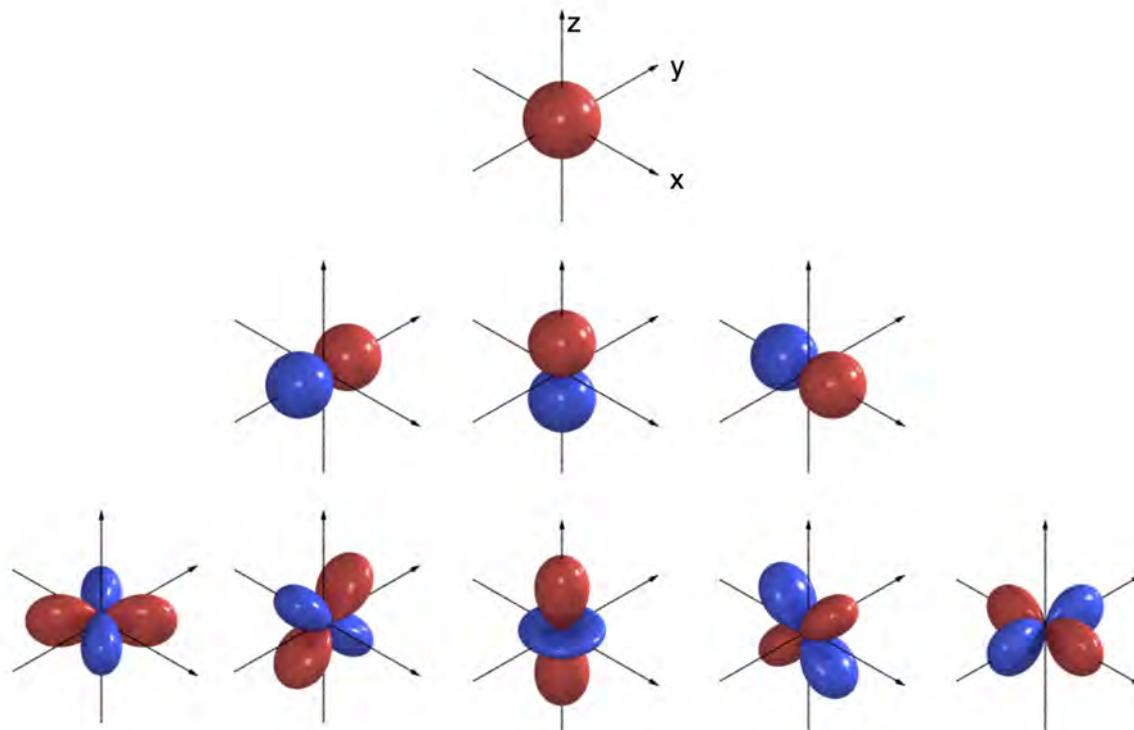
Fig. 17: *The s (first row), p_y, p_z, p_x (second row), and d_{xy}, d_{yz}, $d_{3z^2-r^2}$, d_{xz}, $d_{x^2-y^2}$ (last row) real harmonics.*

Using the definitions $x = r\sin\theta\cos\phi$, $y = r\sin\theta\sin\phi$, $z = r\cos\theta$, we can express the $l = 0, 1, 2$ real harmonics (Fig. 17) as

$$
\begin{aligned}
s &= y_{00} &&= Y_0^0 &&= \sqrt{\tfrac{1}{4\pi}} \\
p_y &= y_{1-1} &&= \tfrac{i}{\sqrt{2}}(Y_1^1 + Y_{-1}^1) = \sqrt{\tfrac{3}{4\pi}} && y/r \\
p_z &= y_{10} &&= Y_2^0 &&= \sqrt{\tfrac{3}{4\pi}} && z/r \\
p_x &= y_{11} &&= \tfrac{1}{\sqrt{2}}(Y_1^1 - Y_{-1}^1) = \sqrt{\tfrac{3}{4\pi}} && x/r \\
d_{xy} &= y_{2-2} &&= \tfrac{i}{\sqrt{2}}(Y_2^2 - Y_{-2}^2) = \sqrt{\tfrac{15}{4\pi}} && xy/r^2 \\
d_{yz} &= y_{2-1} &&= \tfrac{i}{\sqrt{2}}(Y_1^2 + Y_{-1}^2) = \sqrt{\tfrac{15}{4\pi}} && yz/r^2 \\
d_{3z^2-r^2} &= y_{20} &&= Y_2^0 &&= \sqrt{\tfrac{15}{4\pi}}\tfrac{1}{2\sqrt{3}} && (3z^2 - r^2)/r^2 \\
d_{xz} &= y_{21} &&= \tfrac{1}{\sqrt{2}}(Y_1^2 - Y_{-1}^2) = \sqrt{\tfrac{15}{4\pi}} && xz/r^2 \\
d_{x^2-y^2} &= y_{22} &&= \tfrac{1}{\sqrt{2}}(Y_2^2 + Y_{-2}^2) = \sqrt{\tfrac{15}{4\pi}}\tfrac{1}{2} && (x^2 - y^2)/r^2
\end{aligned}
$$

B.3   Slater-Koster integrals

The interatomic Slater-Koster two-center integrals are defined as

$$E_{lm,l'm'} = \int d\boldsymbol{r}\ \overline{\psi_{lm}}(\boldsymbol{r}-\boldsymbol{d})V(\boldsymbol{r}-\boldsymbol{d})\psi_{l'm'}(\boldsymbol{r}).$$

They can be expressed as a function of radial integrals $V_{ll'\alpha}$, which scale with the distance d roughly as $d^{-(l+l'+1)}$ [15], and direction cosines, defined as

$$l = \boldsymbol{d}\cdot\hat{x}/d, \quad m = \boldsymbol{d}\cdot\hat{y}/d, \quad n = \boldsymbol{d}\cdot\hat{z}/d.$$

The Slater-Koster integrals for s-, p-, and d-orbitals [15] are listed below.

$E_{s,s}$	$=$	$V_{ss\sigma}$		
$E_{s,x}$	$=$	$lV_{sp\sigma}$		
$E_{x,x}$	$=$	$l^2V_{pp\sigma}$	$+(1-l^2)V_{pp\pi}$	
$E_{x,y}$	$=$	$lmV_{pp\sigma}$	$-lmV_{pp\pi}$	
$E_{x,z}$	$=$	$lnV_{pp\sigma}$	$-lnV_{pp\pi}$	
$E_{s,xy}$	$=$	$\sqrt{3}lmV_{sd\sigma}$		
E_{s,x^2-y^2}	$=$	$\frac{1}{2}\sqrt{3}(l^2-m^2)V_{sd\sigma}$		
$E_{s,3z^2-r^2}$	$=$	$[n^2-\frac{1}{2}(l^2+m^2)]V_{sd\sigma}$		
$E_{x,xy}$	$=$	$\sqrt{3}l^2mV_{pd\sigma}$	$+m(1-2l^2)V_{pd\pi}$	
$E_{x,yz}$	$=$	$\sqrt{3}lmnV_{pd\sigma}$	$-2lmnV_{pd\pi}$	
$E_{x,zx}$	$=$	$\sqrt{3}l^2nV_{pd\sigma}$	$+n(1-2l^2)V_{pd\pi}$	
E_{x,x^2-y^2}	$=$	$\frac{\sqrt{3}}{2}l[(l^2-m^2)]V_{pd\sigma}$	$+l(1-l^2+m^2)V_{pd\pi}$	
E_{y,x^2-y^2}	$=$	$\frac{\sqrt{3}}{2}m[(l^2-m^2)]V_{pd\sigma}$	$-m(1+l^2-m^2)V_{pd\pi}$	
E_{z,x^2-y^2}	$=$	$\frac{\sqrt{3}}{2}n[(l^2-m^2)]V_{pd\sigma}$	$-n(l^2-m^2)V_{pd\pi}$	
$E_{x,3z^2-r^2}$	$=$	$l[n^2-\frac{1}{2}(l^2+m^2)]V_{pd\sigma}$	$-\sqrt{3}ln^2V_{pd\pi}$	
$E_{y,3z^2-r^2}$	$=$	$m[n^2-\frac{1}{2}(l^2+m^2)]V_{pd\sigma}$	$-\sqrt{3}mn^2V_{pd\pi}$	
$E_{z,3z^2-r^2}$	$=$	$n[n^2-\frac{1}{2}(l^2+m^2)]V_{pd\sigma}$	$+\sqrt{3}n(l^2+m^2)V_{pd\pi}$	
$E_{xy,xy}$	$=$	$3l^2m^2V_{dd\sigma}$	$+(l^2+m^2-4l^2m^2)V_{dd\pi}$	$+(n^2+l^2m^2)V_{dd\delta}$
$E_{xy,yz}$	$=$	$3lm^2nV_{dd\sigma}$	$+ln(1-4m^2)V_{dd\pi}$	$+ln(m^2-1)V_{dd\delta}$
$E_{xy,zx}$	$=$	$3l^2mnV_{dd\sigma}$	$+mn(1-4l^2)V_{dd\pi}$	$+mn(l^2-1)V_{dd\delta}$
E_{xy,x^2-y^2}	$=$	$\frac{3}{2}lm(l^2-m^2)V_{dd\sigma}$	$2lm(m^2-l^2)V_{dd\pi}$	$\frac{1}{2}lm(l^2-m^2)V_{dd\delta}$
E_{yz,x^2-y^2}	$=$	$\frac{3}{2}mn(l^2-m^2)V_{dd\sigma}$	$-mn[1+2(l^2-m^2)]V_{dd\pi}$	$+mn[1+\frac{1}{2}(l^2-m^2)]V_{dd\delta}$
E_{zx,x^2-y^2}	$=$	$\frac{3}{2}nl(l^2-m^2)V_{dd\sigma}$	$+nl[1-2(l^2-m^2)]V_{dd\pi}$	$-nl[1-\frac{1}{2}(l^2-m^2)]V_{dd\delta}$
$E_{xy,3z^2-r^2}$	$=$	$\sqrt{3}lm[n^2-\frac{1}{2}(l^2+m^2)]V_{dd\sigma}$	$-2\sqrt{3}lmn^2V_{dd\pi}$	$\frac{\sqrt{3}}{2}lm(1+n^2)V_{dd\delta}$
$E_{yz,3z^2-r^2}$	$=$	$\sqrt{3}mn[n^2-\frac{1}{2}(l^2+m^2)]V_{dd\sigma}$	$+\sqrt{3}mn(l^2+m^2-n^2)V_{dd\pi}$	$-\frac{\sqrt{3}}{2}mn(l^2+m^2)V_{dd\delta}$
$E_{zx,3z^2-r^2}$	$=$	$\sqrt{3}ln[n^2-\frac{1}{2}(l^2+m^2)]V_{dd\sigma}$	$+\sqrt{3}ln(l^2+m^2-n^2)V_{dd\pi}$	$-\frac{\sqrt{3}}{2}ln(l^2+m^2)V_{dd\delta}$
$E_{x^2-y^2,x^2-y^2}$	$=$	$\frac{3}{4}(l^2-m^2)^2V_{dd\sigma}$	$+[l^2+m^2-(l^2-m^2)^2]V_{dd\pi}$	$+[n^2+\frac{1}{4}(l^2-m^2)^2]V_{dd\delta}$
$E_{x^2-y^2,3z^2-r^2}$	$=$	$\frac{\sqrt{3}}{2}(l^2-m^2)[n^2-\frac{1}{2}(l^2+m^2)]V_{dd\sigma}$	$+\sqrt{3}n^2(m^2-l^2)V_{dd\pi}$	$+\frac{1}{4}\sqrt{3}(1+n^2)(l^2-m^2)V_{dd\delta}$
$E_{3z^2-r^2,3z^2-r^2}$	$=$	$[n^2-\frac{1}{2}(l^2+m^2)]^2V_{dd\sigma}$	$+3n^2(l^2+m^2)V_{dd\pi}$	$\frac{3}{4}(l^2+m^2)^2V_{dd\delta}$

References

[1] J. Kanamori, J. Appl. Phys. **31**, S14 (1960)

[2] K.I. Kugel and D.I. Khomskii, Zh. Eksp. Teor. Fiz. **64**, 1429 (1973)

[3] E. Pavarini, E. Koch, and A.I. Lichtenstein, Phys. Rev. Lett. **101**, 266405 (2008)

[4] E. Pavarini, S. Biermann, A. Poteryaev, A.I. Lichtenstein, A. Georges, O.K. Andersen, Phys. Rev. Lett. **92**, 176403 (2004)
E. Pavarini A. Yamasaki, J. Nuss and O.K. Andersen, New J. Phys. **7**, 188 (2005)

[5] E. Pavarini: *The LDA+DMFT Approach*, in [7]

[6] E. Pavarini and E. Koch, Phys. Rev. Lett. **104**, 086402 (2010)
A. Flesch, G. Zhang, E. Koch, and E. Pavarini, Phys. Rev. B **85**, 035124 (2012)

[7] E. Pavarini, E. Koch, A. Lichtenstein, D. Vollhardt (eds.):
The LDA+DMFT approach to strongly correlated materials,
Reihe Modeling and Simulation, Vol. 1 (Forschungszentrum Jülich, 2011)
http://www.cond-mat.de/events/correl11

[8] E. Pavarini, E. Koch, A. Lichtenstein, D. Vollhardt (eds.):
DMFT at 25: Infinite Dimensions,
Reihe Modeling and Simulation, Vol. 4 (Forschungszentrum Jülich, 2014)
http://www.cond-mat.de/events/correl14

[9] E. Pavarini, E. Koch, F. Anders, M. Jarrell (eds.):
Correlated Electrons: From Models to Materials,
Reihe Modeling and Simulation, Vol. 2 (Forschungszentrum Jülich, 2012)
http://www.cond-mat.de/events/correl12

[10] V.I. Anisimov, F. Aryasetiawan and A.I. Lichtenstein, J. Phys. Cond. Mat. **9**, 767 (1997)

[11] W.G. Yin, D. Volja, and W. Ku, Phys. Rev. Lett. **96**, 116405 (2006)

[12] I. Leonov, N. Binggeli, Dm. Korotin, V.I. Anisimov, and D. Vollhardt, Phys. Rev. Lett. **101**, 096405 (2008); I. Leonov, Dm. Korotin, N. Binggeli, V.I. Anisimov, and D. Vollhardt Phys. Rev. B **81**, 075109 (2010)

[13] K.H. Ahn, and A.J. Millis, Phys. Rev. B **61**, 13545 (2000)

[14] M.C. Sánchez, G. Subías, J. García, and J. Blasco, Phys. Rev. Lett. **90**, 045503 (2003)

[15] W.A. Harrison: *Electronic Structure and The Properties of Solids* (Dover, 1989)